Kinetic Characterization and Inhibition of *Trypanosoma cruzi* Hypoxanthine−Guanine Phosphoribosyltransferases

Kayla Glockzin, Demetrios Kostomiris, Yacoba V. T. Minnow, Kajitha Suthagar, Keith Clinch, Sinan Gai, Joshua N. Buckler, Vern L. Schramm, Peter C. Tyler, Thomas D. Meek,* and Ardala Katzfuss*
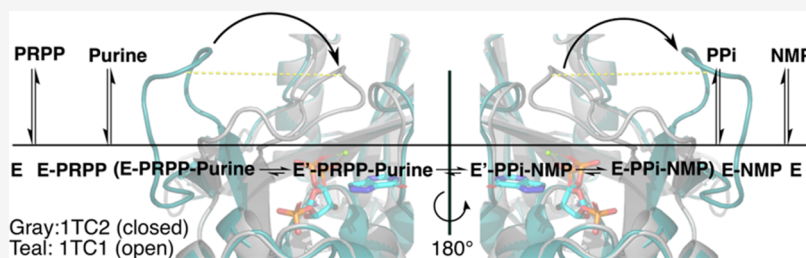
Cite This: *Biochemistry* 2022, 61, 2088−2105

Read Online

ACCESS | Metrics & More | Article Recommendations | Supporting Information

Gray:1TC2 (closed)
Teal: 1TC1 (open)

ABSTRACT: Chagas disease, caused by the parasitic protozoan *Trypanosoma cruzi*, affects over 8 million people worldwide. Current antiparasitic treatments for Chagas disease are ineffective in treating advanced, chronic stages of the disease, and are noted for their toxicity. Like most parasitic protozoa, *T. cruzi* is unable to synthesize purines *de novo*, and relies on the salvage of preformed purines from the host. Hypoxanthine−guanine phosphoribosyltransferases (HGPRTs) are enzymes that are critical for the salvage of preformed purines, catalyzing the formation of inosine monophosphate (IMP) and guanosine monophosphate (GMP) from the nucleobases hypoxanthine and guanine, respectively. Due to the central role of HGPRTs in purine salvage, these enzymes are promising targets for the development of new treatment methods for Chagas disease. In this study, we characterized two gene products in the *T. cruzi* CL Brener strain that encodes enzymes with functionally identical HGPRT activities *in vitro*: TcA (TcCLB.509693.70) and TcC (TcCLB.506457.30). The TcC isozyme was kinetically characterized to reveal mechanistic details on catalysis, including identification of the rate-limiting step(s) of catalysis. Furthermore, we identified and characterized inhibitors of *T. cruzi* HGPRTs originally developed as transition-state analogue inhibitors (TSAIs) of *Plasmodium falciparum* hypoxanthine−guanine−xanthine phosphoribosyltransferase (*Pf*HGXPRT), where the most potent compound bound to *T. cruzi* HGPRT with low nanomolar affinity. Our results validated the repurposing of TSAIs to serve as selective inhibitors for orthologous molecular targets, where primary and secondary structures as well as putatively common chemical mechanisms are conserved.

INTRODUCTION

Over 8 million people are infected with Chagas disease (CD) worldwide.[1] CD primarily affects rural areas of 21 endemic countries in Latin America such as Mexico, El Salvador, Guatemala, and Honduras, with more than 70 million people at risk of infection.[2] Notwithstanding, the Center for Disease Control estimates there are over 300,000 cases of CD in the U.S.,[1] and widespread serological screening of blood donor samples revealed cases in 42 states in the U.S., with higher rates in California, Texas, and Florida.[3] Current treatment for CD relies on the antiparasitic drug benznidazole, and to a lesser extent nifurtimox, both of which are replete with side effects, and are only effective during the acute phase of infection.[4] The drug regimen requires as many as 60 days during which the severity of side effects of benznidazole and nifurtimox frequently leads to the abandonment of treatment.[5−7] The acute phase of CD often presents with low mortality and symptomatology, and consequently, patients can remain asymptomatic for years while unaware of their infected status, thereby contributing to CD spread.[8] As the disease progresses into the chronic stage, it is generally considered to be incurable, and roughly 30% of chronic patients develop debilitating damage to the cardiovascular system. As many as 10% of patients at this point develop digestive, neurological, and/or cardiomyopathic pathologies, including megavisceras.[5−7,9,10] Thus, novel therapies that are effective against both acute and chronic stages of CD are urgently needed.
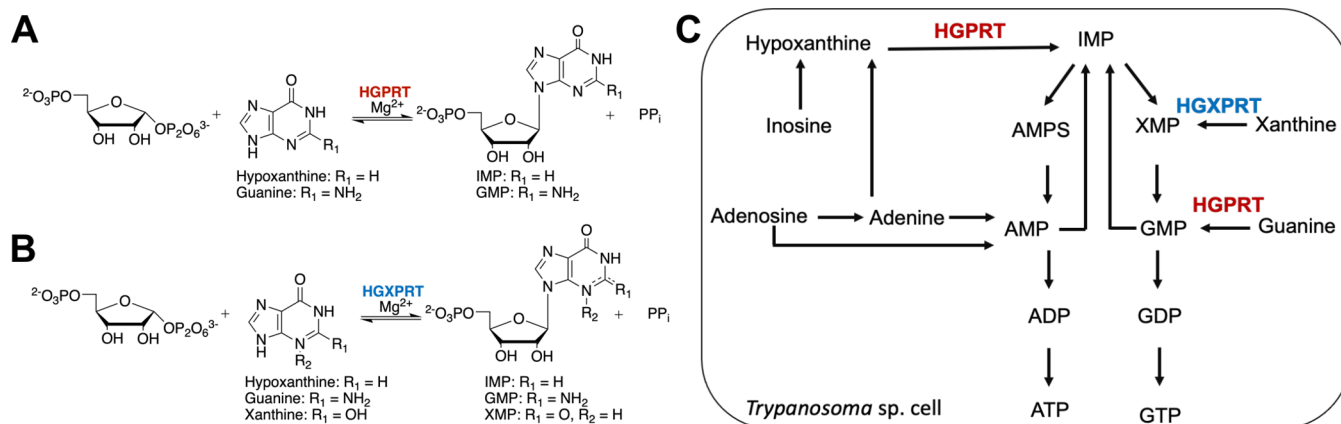
Apart from the social, economic, and political factors that diminish the research and development of novel drugs for the treatment of all neglected tropical diseases,[11,12] the intrinsic complexities of the life cycle of CD's etiological agent—
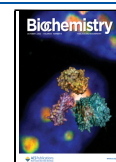
Figure 1. Reactions catalyzed by (A) HGPRT, EC 2.4.2.8. and (B) HGXPRT, EC 2.4.2.8. (C) Purine metabolism in *Trypanosoma* sp. Reactions catalyzed by HGPRT and HGXPRT are depicted in red or blue text, respectively, over the reaction arrow. IMP: inosine monophosphate, AMPS: adenylosuccinate, AMP: adenosine monophosphate, ADP: adenosine diphosphate, ATP: adenosine triphosphate, XMP: xanthosine monophosphate, GMP: guanosine monophosphate, GDP: guanosine diphosphate, and GTP: guanosine triphosphate.

Trypanosoma cruzi[13−18]—exacerbate the challenges in developing specific and selective therapies against this important disease. *T. cruzi* known genetic plasticity and variable gene expression along its life cycle[8,19] is linked to its ability to evade the host's immune system.[20−23]

T. cruzi, like other parasitic protozoa, is an obligatory purine auxotroph that lacks a functional *de novo* synthetic pathway to make purine nucleotides.[24] Instead, the parasite relies exclusively on salvage pathways in which the uptake of preformed purines from its hosts occurs by a highly selective nucleobase/proton symporter system.[25] Purine phosphoribosyltransferases (PPRTs) convert purines into nucleotide monophosphates (NMPs). Hypoxanthine−guanine phosphoribosyltransferases (HGPRTs, EC 2.4.2.8) are among the essential enzymes of the purine salvage pathway, which catalyze the magnesium-dependent formation of guanosine monophosphate (GMP) and inosine monophosphate (IMP) from 5-phospho-α-D-ribose 1-diphosphate (PRPP; the Mg·PRPP complex is the enzyme's actual substrate[26]) and the 6-oxopurines guanine (Gua) and hypoxanthine (Hx), respectively (Figure 1). Notably, IMP is positioned at the branching point of the salvage pathway and can be converted into XMP, GMP, or adenosine monophosphate (AMP) (Figure 1C). The HGPRTs are thus promising drug targets because of their central importance in nucleotide biosynthesis in *T. cruzi*.[27−30] Noteworthy, a previous study showed that 19 *T. cruzi* strains susceptible to benznidazole and nifurtimox treatment *in vivo* were polymorphic for HGPRT,[27] indicating a direct correlation between *T. cruzi* HGPRT polymorphism and drug susceptibility. The expression of HGPRTs along the life cycle of the closely related organism *Trypanosoma brucei* indicates its presence in both human and insect host stages,[31] as expected for their essential roles in purine base incorporation, thus supporting its value as a viable drug target.

The clone referenced in the *T. cruzi* annotated genome, CL Brener, is a hybrid composed of two relatively distinct parental lineages: Esmeraldo and non-Esmeraldo.[32] *T. cruzi* CL Brener has a pair of genes encoding putative HGPRT enzymes: TcCLB.509693.70 and TcCLB.506457.30, named herein, respectively, TcA and TcC. TcA is derived from the non-Esmeraldo parental strain, while TcC is derived from the Esmeraldo parental strain. TcA and TcC share high primary sequence identity (>98%) with only three amino acids

difference (TcA to TcC: K24M, C67S, L87V—Figure S1). The *T. cruzi* genome also encodes two hypoxanthine−guanine−xanthine phosphoribosyltransferases (HGXPRTs, EC 2.4.2.8), similarly derived from both the Esmeraldo and non-Esmeraldo parental strains (TcCLB.509693.80 and TcCLB.506457.40). These enzymes are also capable of catalyzing the conversion of xanthine (Xan) to XMP in addition to using Hx and Gua as substrates (Figure 1B,C). Studies of RNAi silencing in *T. brucei* indicated that the combined and overlapping activities of HGPRTs and HGXPRTs are essential for the parasite's survival *in vitro*,[31] highlighting the importance of PPRTs as drug targets for the treatment of CD. The data presented in this manuscript focus on the HGPRT isoforms, TcA and TcC.

Our results indicate that the two HGPRTs, TcA and TcC, are functionally equivalent, with both enzymes having essentially identical kinetic data, in agreement to what has been previously described for the TcA isoform.[33−35] We further sought to characterize the kinetic and chemical mechanisms of the TcC isoform and identify potent inhibitors of *T. cruzi* HGPRTs. We exploited the structural and catalytic similarities between *T. cruzi* HGPRTs and the single HGXPRT from *Plasmodium falciparum* (*Pf*HGXPRT) to repurpose previously described, exceptionally potent, transition-state analogue inhibitors (TSAIs) of *Pf*HGXPRT as potential lead molecules to treat CD.[36,37] *P. falciparum*, the main causative agent of malaria, is also a parasitic protozoa and an obligatory purine auxotroph.[38,39] Our results revealed that TSAIs of *Pf*HGXPRT were also excellent inhibitors of *T. cruzi* HGPRTs, the most potent of which exhibited low nanomolar affinity.
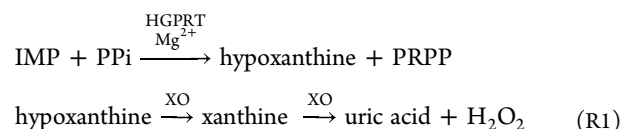
■ MATERIALS AND METHODS

Unless otherwise indicated, all biochemicals were purchased from Sigma-Aldrich/Sigma Millipore (Burlington, MA). Concentrations of PRPP within solutions made from commercial PRPP were corrected for its purity as indicated by the supplier (75% purity).

Expression and Purification of *T. cruzi* HGPRTs: TcA and TcC, EC 2.4.2.8. The coding sequences of TcA (TcCLB.509693.70, NCBI XP_816916) and TcC (TcCLB.506457.30, NCBI XP_813396) were codon-optimized for expression in *Escherichia coli*, synthesized, and cloned into a pET-28a(+) expression vector using *Nde*I and *Hind*III restriction sites (GenScript) in which a His₆ sequence was

encoded upstream of the N-terminus of the coding sequences. Optimal expression of TcA and TcC was obtained in C43(DE3) cells, grown in Terrific Broth (TB) media. The plasmids pET-28a(+)::TcA and pET-28a(+)::TcC were individually transformed into C43(DE3) cells by heat shock and incubated overnight on plates containing 50 μg mL^{-1} of kanamycin at 37 °C. A single colony of each strain was used to inoculate a 50 mL starter culture of TB media in the presence of 50 μg mL^{-1} kanamycin. Starting cultures were incubated overnight at 37 °C in an orbital shaker set at 180 rpm. Thirteen milliliters of starting culture were used to inoculate 500 mL of TB media in the presence of kanamycin 50 μg mL^{-1}. Cultures were grown at 37 °C and set to 180 rpm until an OD$_{600}$ of 0.4−0.6 was reached. Protein expression was induced by the addition of 1 mM isopropyl β-D-1-thiogalactopyranoside (IPTG) (final concentration). Cells were further grown under these conditions for 24 h. Cells were harvested by centrifugation at 5,000 rpm for 45 min at 4 °C. Cell pellets were stored at −20 °C until purification. Cell pellets were resuspended in buffer A (50 mM Na$_2$HPO$_4$/NaH$_2$PO$_4$, pH 7.4, 300 mM NaCl). Lysozyme was added at a final concentration of 0.2 mg mL^{-1}, and cells were disrupted by sonication (60% amplitude for 15 cycles of 10 s each). Cell lysates were then clarified by centrifugation (18,000 rpm for 45 min at 4 °C). The His-tagged proteins were purified using HisPur Ni-NTA resin (Thermo Fisher Scientific), preequilibrated with Buffer A containing 10 mM imidazole (equilibration buffer) at room temperature (RT). The resin was washed with 5 column volumes (CV) of equilibration buffer, followed by 5 CV of buffer A containing 20 mM imidazole, followed by 2 CV of buffer A containing 50 mM imidazole. The protein was eluted with a 300−600 mM imidazole stepwise gradient over 25 CV of buffer A. The first 2 CV were discarded. Fractions containing the proteins of interest, as inferred by analysis with 12% sodium dodecyl sulfate-polyacrylamide gel electrophoresis (SDS-PAGE) stained with Coomassie Blue (Figure S2), were pooled and dialyzed against 50 mM N-(2-hydroxyethyl)piperazine-N'-(3-propanesulfonic acid) (EPPS) (pH 8.3), 500 mM NaCl, 50 mM L-arginine, and 50 mM L-glutamate at 4 °C using 12−14 kDa molecular weight cutoff (MWCO) dialysis membranes (Spectrum Spectra/Por 4 regenerated cellulose). Homogeneous recombinant proteins were stored in the presence of 10% (v/v) glycerol at −80 °C.

Analytical Size-Exclusion Chromatography (SEC) of Purified TcA and TcC. To verify the oligomeric state and to ensure purified protein is not aggregated, TcA and TcC were subjected to SEC. The purified proteins were first concentrated to 14.6 and 14.1 mg mL^{-1}, respectively. Concentrated TcA or TcC (200 μL) was applied to a column (GE Superdex 200 Increase 10/300 GL), preequilibrated with SEC buffer (50 mM N-(2-hydroxyethyl)piperazine-N'-ethanesulfonic acid (HEPES) pH 7.8, 300 mM NaCl, 50 mM L-arginine, 50 mM L-glutamate). Chromatography was performed on an ÄKTA pure system (GE Healthcare). Proteins were eluted off with 1.2 CV of SEC buffer at a flow rate of 0.35 mL min^{-1}. Prior to sample application, the column was calibrated with lyophilized protein standards resuspended in SEC buffer, including thyroglobulin (670 kDa), bovine γ-globulin (158 kDa), chicken ovalbumin (44 kDa), equine myoglobin (17 kDa), and vitamin B12 (1.3 kDa) (BioRad, Cat #1511901). Blue dextran (15 mg mL^{-1}) was used to measure the void volume of the column. Samples were compared to the standards to ascertain the M_r (relative molecular weight).

Kinetic Assays for Measuring HGXPRT Activity. Steady-state kinetic assays for the forward (biosynthetic) and reverse reactions of HGPRT and HGXPRT were measured using continuous spectrophotometric assays. All assays were carried out in an assay buffer (50 mM EPPS, pH 8.3, 12 mM MgCl$_2$) unless otherwise noted. Reaction mixtures (final volume, 250 μL) were added to Greiner Bio-One UV-Star 96-well microplates, and absorbance was measured using a BioTek Synergy HTX plate reader. The biosynthetic reaction was measured as previously described.[38,40] Briefly, formation of IMP, GMP, and XMP was monitored at 245, 257.5, and 253 nm, respectively ($\Delta\varepsilon_{245}$ = 1,227 M^{-1} cm^{-1}, $\Delta\varepsilon_{257.5}$ = 4,044 M^{-1} cm^{-1}, $\Delta\varepsilon_{253}$ = 4,250 M^{-1} cm^{-1}). The apparent kinetic parameters of allopurinol (4-hydroxypyrazolo(3,4-d)pyrimidine or HPP) as a substrate for TcC were also determined. The absorbance spectra of the reaction product, HPP monophosphate, is sufficiently different from the substrate HPP, thereby providing a continuous spectrophotometric assay. Calibration curves were prepared from spectrophotometric data of reaction mixtures in which known concentrations of HPP were incubated with apparent saturating concentrations of PRPP (1 mM) and 1 μM TcC in the assay buffer for 10 min, allowing the quantitative conversion to HPP monophosphate. Calibration curves were also prepared with known concentrations of HPP in the assay buffer. The differences in absorbance of HPP monophosphate and HPP were measured at 272 nm for which the difference in extinction coefficient of the riboside product was determined to be $\Delta\varepsilon_{272}$ = 1,533 M^{-1} cm^{-1}. The reverse reaction was monitored by coupling the formation of Hx to commercially available xanthine oxidase (XO, EC 1.17.3.2; reaction R1). The same assay buffer was used to assay the reverse direction, with the addition of 1.28 U mL^{-1} XO to the reaction mixture. Uric acid formation was monitored at 293 nm ($\Delta\varepsilon_{293}$ = 12,600 M^{-1} cm^{-1})[41]

$$\text{IMP} + \text{PPi} \xrightarrow[\text{Mg}^{2+}]{\text{HGPRT}} \text{hypoxanthine} + \text{PRPP}$$

$$\text{hypoxanthine} \xrightarrow{\text{XO}} \text{xanthine} \xrightarrow{\text{XO}} \text{uric acid} + \text{H}_2\text{O}_2 \qquad \text{(R1)}$$

Apparent kinetic parameters for TcA (25 nM) and TcC (6 nM) (appK_m, appk_{cat}, and appk_{cat}/K_m) were determined from initial velocity measurements in triplicate with at least seven concentrations of variable substrate, and at apparent, fixed saturating concentrations of the second substrate in the assay buffer. Apparent kinetic parameters for the 6-oxopurines were determined with reaction mixtures containing variable concentrations of Hx (5−150 μM), Gua (5−200 μM), or Xan (50−500 μM) in the presence of an apparent saturating concentration of PRPP (1 mM). Apparent kinetic parameters for PRPP were determined with reaction mixtures containing variable concentrations of PRPP (6−200 μM) and at apparent saturating, fixed concentrations of Hx (100 μM) or Gua (100 μM). Apparent kinetic parameters for HPP were likewise determined with reaction mixtures containing apparent saturating, fixed concentrations of PRPP (1 mM) and variable concentrations of HPP (50−700 μM). The apparent kinetic parameters were calculated by fitting of initial rate data to eq 1. An initial velocity study of the reverse reaction for recombinant TcC (11.4−45.6 nM) of pyrophosphate (PPi) (12−250 μM) vs variable IMP (31−1000 μM) was performed, and data were fit to eq 2.

Product Inhibition Studies. Product inhibition studies of the reverse reaction (PRPP vs IMP) were conducted in assay

mixtures containing apparent saturating concentrations of PPi (100 μM), variable concentrations of IMP (12.5−500 μM), fixed concentrations of PRPP (0, 0.5, 1, and 3 μM), and 25 nM TcC in the assay buffer. The inhibition pattern of PRPP vs IMP was determined with initial velocity data plotted in double-reciprocal form, and fitting of these data to eqs 3−5 to determine if product inhibition was competitive, noncompetitive, or uncompetitive. Product inhibition studies of the forward reaction, IMP vs PRPP and GMP vs PRPP, were conducted in assay mixtures containing fixed, apparent saturating concentrations of Gua (50 μM), variable concentrations of PRPP (10−200 μM), fixed concentrations of either GMP (0, 15, and 60 μM) or IMP (0, 60, and 120 μM), and 6 nM TcC in the assay buffer. The inhibition patterns of IMP vs PRPP and GMP vs PRPP were obtained, and data were fit to eqs 3−5 to ascertain modes of inhibition. Formation of products IMP and GMP was measured spectrophotometrically as previously described for the HGPRT forward activity assays. Hx formation was measured as previously described for the HGPRT reverse-coupled assay.

Isothermal Titration Calorimetry (ITC) Binding Assays. ITC binding assays were carried out at 25 °C using a MicroCal iTC200 microcalorimeter. The reference cell (200 μL) was loaded with Milli-Q water during all assays, and the sample cell (280 μL) contained 282 μM TcC. The injection syringe (39.7 μL) was filled with the substrate or product at different concentrations: 3.83 mM PRPP, 7.5 mM Hx, 10 mM PPi, and 6 mM IMP. The ligand binding isotherms were measured by direct titration (ligand into macromolecule). Control titrations (ligand into buffer) were performed to subtract the heat of dilution and mixing for each experiment prior to data analysis. The first injection (0.5 μL) of ligand was followed by 15 injections (2.49 μL) separated by 180 s. The reference power was set to 11 μcal s^{-1} and the stirring speed was set to 750 rpm. The titration value of the first injection was discarded from data analysis. TcC and all ligand solutions contained 50 mM EPPS (pH 8.0), 500 mM NaCl, 12 mM MgCl$_2$, 50 mM L-arginine, and 50 mM L-glutamate. The heat variation was measured inside the sample cell, allowing the determination of the binding enthalpy ($\Delta H°$), the association constant (K_a), and the number of binding sites per monomer (N). ITC data were fit to the one-set-of-sites model.[42] The Gibbs free energy ($\Delta G°$) and the entropy ($-T\Delta S°$) of binding were calculated using the relationship described in eq 7, and K_d was calculated as the inverse of K_a.

Viscosity Studies. The effects of viscosity on the forward reaction of TcC were determined by measuring its initial velocity in the presence of 0, 4, 8, and 12% (v/v) glycerol (micro-viscosogen; relative viscosities (η_{rel}) = 1−1.45) or 0, 0.5, 1, and 2% (w/v) PEG$_{10000}$ (macroviscosogen; η_{rel} = 1−1.46). The kinematic viscosity of the reaction mixtures containing glycerol was measured using a Cannon−Fenske viscometer (capillary no. 100), and η_{rel} was calculated using eq 8. Kinematic viscosities were converted to dynamic viscosities (absolute viscosity, reflecting internal resistance of the fluid) using eq 9. η_{rel} values were calculated using the relationship described in eq 10. Kinetic data were collected in triplicate for reaction mixtures containing 6 nM TcC, 20 μM Hx, varied PRPP (0−200 μM), and fixed concentrations of glycerol (0, 4, 8, and 12% v/v) or PEG$_{10000}$ (0, 0.5, 1.0, and 2.0% w/v) in the assay buffer. IMP formation was measured as previously described for the HGPRT activity assays. Kinetic parameters were determined by fitting the initial velocity data to eq 1, to afford the apparent kinetic parameters (k_{cat}, K_{PRPP}, and k_{cat}/K_{PRPP}) at each of the values of η_{rel}. Data were plotted as the normalized kinetic parameter (i.e., $[k_{cat}/(k_{cat})_\eta]$ or

$[(k_{cat}/K_{PRPP})/(k_{cat}/K_{PRPP,\eta})]$) as a function of η_{rel}, and fit to eq 11 in which the slope represents the dependence on viscosity on the normalized kinetic parameter.[43]

Expression and Purification of *T. brucei brucei* Adenine Phosphoribosyltransferase 1 (*Tbb*APRT1, EC 2.4.2.7). *Tbb*APRT1 was expressed and purified as previously described.[44] In brief, the coding sequence of *Tbb*APRT1 (Tbb927.7.1780, UniProt Q57V32) was codon-optimized for expression in *E. coli* and cloned into a pET-28a(+) vector, using *Nde*I and *Hin*dIII restriction sites (Genscript), containing an N-terminal His-tag. Optimal expression of *Tbb*APRT1 was obtained in BL21(DE3) cells using TB media. The plasmid pET-28a(+)::*aprt1* was transformed into BL21(DE3) cells by heat shock, and plates containing kanamycin 50 μg mL^{-1} were incubated overnight at 37 °C. *Tbb*APRT1 expression, cell harvesting and storage, and recombinant enzyme purification were performed following the protocol described above for TcA and TcC. Fractions containing apparently homogeneous *Tbb*APRT1, as inferred by SDS-PAGE (12% polyacrylamide; stained with Coomassie Blue), were pooled and dialyzed against 50 mM EPPS (pH 8.0), 300 mM NaCl. Homogeneous recombinant proteins were stored in the presence of 10% (v/v) glycerol at −80 °C.

Expression and Purification of *Saccharomyces cerevisiae* Adenine Deaminase (*Sc*ADE, EC 3.5.4.2). The coding sequence of the zinc-dependent adenine deaminase from *S. cerevisiae* (*Sc*ADE), encoded by the gene *aah1* (UniProt P53909), was codon-optimized for expression in *E. coli* and cloned into a pET-28a(+)-TEV expression vector using *Nde*I and *Hin*dIII restriction sites (GenScript) in which a His$_6$ sequence was encoded upstream of the N-terminus of the coding sequences. Optimal expression of *Sc*ADE was obtained in BL21(DE3) cells using TB media. The plasmid pET-28a(+)-TEV::*aah1* was transformed into BL21(DE3) cells by heat shock, and plates containing kanamycin 50 μg mL^{-1} were incubated overnight at 37 °C. *Sc*ADE expression, cell harvesting, storage, and recombinant enzyme purification were performed as described above for TcA and TcC. Fractions containing apparently homogeneous *Sc*ADE, as inferred by SDS-PAGE (12% polyacrylamide; stained with Coomassie Blue), were pooled and dialyzed against 50 mM EPPS (pH 8.0), 300 mM NaCl. Homogeneous recombinant proteins were stored in the presence of 10% (v/v) glycerol at −80 °C.

Synthesis of Radiolabeled PRPP. [1′-^{3}H]-, [1′-^{14}C]-, [5′-^{3}H]-, and [5′-^{14}C]AMP were synthesized and converted into radiolabeled PRPP by enzymatic synthesis utilizing *Tbb*APRT1 and *Sc*ADE as previously described[45] (Figure S3). Briefly, 50 mM potassium phosphate (pH 7.4), 1.4 mM MgCl$_2$, 1.4 mM PPi, 0.5 mM dithiothreitol (DTT), 35 μM purified *Tbb*APRT1, and 0.2 mg mL^{-1} *Sc*ADE (final concentration) were added to a 1.5 mL microcentrifuge tube at RT. Radiolabeled AMP (50 μM) was added to start the reaction. After a 15 min incubation at RT, the reaction was quenched by the addition of ethylenediamine-tetraacetic acid (EDTA) (final concentration 6.4 mM). The quenched reaction was filtered by centrifugation using a microcentrifuge spin column (Millipore Sigma Amicon Ultra, 0.5 mL 10 kDa MWCO). The sample was then injected on to a 5 mL anion exchange Mono Q column (GE Life Science) preequilibrated with deionized water. Material was eluted by a linear gradient (0−1.5 M) of ammonium acetate at a flow rate of 1 mL min^{-1} and 2 mL fractions were collected. Fractions were analyzed by liquid scintillation counting (LSC; Tricarb, PerkinElmer) after the addition of 25−50 μL of each fraction

to 10 mL of Ultima Gold scintillation fluid. Chromatographic fractions that corresponded to PRPP were pooled together and diluted with Milli-Q water (3:4 water/sample). The radio-labeled PRPP sample was then frozen with liquid nitrogen, lyophilized to dryness, and then resuspended in 3 mL of Milli-Q water. A 25−50 μL aliquot was removed for LSC, and the sample was again flash frozen with liquid nitrogen and lyophilized to dryness. Dried samples were stored at −20 °C.

Isotope Partitioning and Determination of Commitment to Catalysis. The specific radioactivity of preparative samples of [5-^{3}H]PRPP was determined through titration and purification. A master mix of 2.15 μM TcC and 2.18×10^3 counts per minute (cpm) μL^{-1} of [5-^{3}H]PRPP in the assay buffer was pipetted into 10 μL aliquots. Ten microliters of Hx (dissolved in the assay buffer) was added to each aliquot to a final concentration of 0−4 μM. After a brief incubation (<10 min), 480 μL of a chase solution was added containing 1.05 mM unlabeled PRPP in the assay buffer. The reactions were quenched with the addition of 125 μL of 100 mM EDTA, and the quenched solutions were applied to an ion exchange column (Mono Q, 5 mL), and radiolabeled products were isolated as described for the kinetic isotope effects (KIEs) below. Fractions that eluted at the same retention time as IMP (t_R = 13.2 min) were pooled and lyophilized as described above for the synthesis of radiolabeled PRPP. Ten milliliters of Ultima Gold scintillation fluid was added to the lyophilized residues, and the samples were analyzed by LSC. Sample quenching and disintegrations per minute (dpm) were calculated by the tSIE parameter (external standard quench parameter) and referenced to a quench standard curve (Figure S4).[46]

Isotope partitioning (trapping) experiments were performed according to the method of Rose *et al.*[47,48] with some modifications. TcC was buffer-exchanged by chromatography (GE Healthcare, PD MidiTrap G-25) with elution by the assay buffer. A pulse solution containing 4.34 μM [5-^{3}H]PRPP, 10 μM TcC, and assay buffer was divided into 20 μL aliquots. 480 μL of chase solution containing 1.04 mM unlabeled PRPP, 0−75 μM Hx, and assay buffer was added to each pulse solution with rapid mixing. The pulse-chase mixture was then quenched by the addition of 125 μL of 100 mM EDTA and then placed on ice prior to purification of the radiolabeled products by ion-pairing HPLC as described above. Fractions containing IMP were then lyophilized, and radioactivity was determined by LSC. The amount of the radiolabeled EA* complex (TcC-PRPP*) present in the pulse mixtures was calculated by the K_{is} constant of PRPP (Table 4, 0.8 ± 0.1 μM) and the radioactivity (dpm) in the PRPP sample. The radioactivity in the sample from degradation products that coeluted with IMP (in samples lacking Hx) was subtracted from the total counts. The data for the isotope trapping was fit to eq 14, providing an approximation for the commitment of the binary TcC-PRPP* complex to form labeled IMP (IMP*) at varying concentrations of Hx.

Kinetic Isotope Effects (KIEs). KIEs were measured by internal competition:[49] heavy (^{3}H and ^{14}C) and light (^{1}H and ^{12}C) atoms were measured in the same samples, employing the remote-labeling method. The remote label is [5-^{3}H]PRPP for [1-^{14}C]PRPP KIEs and [5-^{14}C]PRPP for [1-^{3}H]PRPP KIEs,[49,50] and the ratios of heavy to light atoms were compared in either the product (NMP) or the substrate (Hx or HPP). Reaction mixtures containing ~10 μM radiolabeled PRPP (^{3}H/^{14}C = 3:1 dpm) and 6-oxopurine (final concentration of 10 or 50 μM for Hx and 190 μM for HPP) in 50 mM potassium phosphate (pH 7.4), 1.4 mM MgCl$_2$, and 0.1 mM DTT

(reaction buffer) were aliquoted into separate tubes. TcC (100 nM) or water (control) was added to aliquots to initiate the reaction. After a 5 min incubation, the reaction mixtures containing TcC were quenched by the addition of EDTA (14.3 mM, final concentration), while control samples were quenched without any incubation. The quenched samples were filtered using a 10 kDa MWCO microcentrifuge filter (Millipore Sigma Amicon Ultra 0.5 mL) and injected onto a Phenomenex 250 mm Luna C18 (5 μm) column preequilibrated with aqueous ion-pairing buffer (25 mM potassium phosphate, pH 6.0, 4 mM tetrabutylammonium bisulfate). The nucleotide products were separated from remaining radiolabeled PRPP and other degradation products as previously described,[45,51] with some modifications (Figure S5). Briefly, radiolabeled substrates and products were separated by a linear gradient of 0−30% acetonitrile at a flow rate of 1 mL min^{-1}. Fractions of 1 mL were collected, and 50 μL aliquots were added to 10 mL of Ultima Gold scintillation fluid, followed by LSC. Samples were counted for 10 min, and samples with more than 100 cpm were counted 10 times for 10 min in which a 0.5% 2 CV cutoff was used. Scintillation counting was evaluated in two different channels: channel A contained counts of 0−26 keV energy, and channel B contained counts of 26−1000 keV energy. Initial radioactivity in the substrate was measured in a control sample that did not contain the enzyme. After a fraction of reaction (f) of the total substrate was converted to the product (f = 0.35−0.80), radioactivity in both the residual substrate and formed product was measured. Radioactivity (cpm) corresponding to ^{3}H and ^{14}C was calculated by the relationship described in eq 16, and KIEs were calculated using eq 17. KIEs were measured in the product and residual substrate.

Synthesis of *T. cruzi* HGPRT Inhibitors. Immucillin-HP (**8**), Immucillin-GP (**9**), and compounds (**S**)-**2**, (**R**)-**2**, **3**, **6**, **7**, and **11** were synthesized as previously described.[52,53] Synthesis of **4** was performed as described in Scheme S1. Synthesis of **12** was performed as described in Schemes S2 and S3. Synthesis of compound **10** was performed as described in Scheme S4. Synthesis of compounds **1** and **5** was performed as described in Schemes S5 and S6.

Screening of *T. cruzi* HGPRT Inhibitors. The potency of *T. cruzi* HGPRT inhibitors was assessed for inhibitory activity in assays containing 120 μM Hx, 1 mM PRPP, variable concentrations of inhibitor (0−100 μM), and 20 nM TcC in which IMP formation was measured as previously described. The apparent potency of *T. cruzi* HGPRT inhibitors (IC_{50}) was determined with initial velocity data fit to eq 18. Inhibition constants (K_i) were determined using the relationship described in eq 19. Inhibition patterns (competitive, uncompetitive, or noncompetitive) were determined with concentration−response curves performed with 30, 60, 90, 120, and 180 μM Hx in the presence of 1 mM PRPP, and 15 nM TcC at fixed levels of inhibitors. Double-reciprocal plots of inhibitors *vs* Hx for TcC were obtained, and data were fit to eqs 3−5 to determine the pattern of inhibition. The selectivity index (SI) was calculated as the appK_i for human HGPRT (*Hs*HGPRT) divided by the appK_i for *T. cruzi* HGPRT.

Expression and Purification of *Pf*HGXPRT, *Hs*HGPRT, and *Streptococcus pyogenes* Inosine 5′-Monophosphate Dehydrogenase (*Sp*IMPDH, EC. 1.1.1.205). *Pf*HGXPRT was expressed and purified as previously described.[45] Briefly, a thrombin-cleavable N-terminal His$_6$ tag was encoded in the open reading frame and inserted into pDEST-14. The plasmid was overexpressed in *E. coli* One Shot BL21-AI competent cells

Table 1. Equations Used for Data Analysis

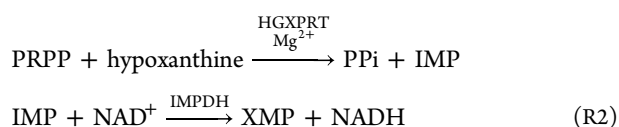| eq #	equation
1	$\dfrac{v}{E_t} = \dfrac{k_{cat}A}{K_a + A}$ (1)
2	$\dfrac{v}{E_t} = \dfrac{k_{cat}AB}{K_{ia}K_b + K_bA + K_aB + AB}$ (2)
3	$\dfrac{v}{E_t} = \dfrac{k_{cat}A}{K_a\left(1 + \frac{I}{K_{is}}\right) + A}$ (3)
4	$\dfrac{v}{E_t} = \dfrac{k_{cat}A}{K_a\left(1 + \frac{I}{K_{is}}\right) + A\left(1 + \frac{I}{K_{ii}}\right)}$ (4)
5	$\dfrac{v}{E_t} = \dfrac{k_{cat}A}{K_a + A\left(1 + \frac{I}{K_{ii}}\right)}$ (5)
6	$K_{eq} = \dfrac{V_{max,f}K_{iq}K_P}{V_{max,r}K_{ia}K_b}$ (6)
7	$\Delta G^{\circ} = -RT \ln K_a = \Delta H^{\circ} - T\Delta S^{\circ}$ (7)
8	$\eta_{kinematic} = tK$ (8)
9	$\eta_{dynamic} = \eta_{kinematic}d$ (9)
10	$\eta_{relative} = \dfrac{\eta_x}{\eta_0}$ (10)
11	$\dfrac{k}{k_\eta} = m(\eta_{rel} - 1) + 1$ (11)
12	$\log\left(\dfrac{k_{cat}}{k_{cat,\eta}}\right) = m(\log(\eta_{rel}))$ (12)
13	${}^x\left(\dfrac{V}{K_{PRPP}}\right) = \dfrac{{}^xk_7 + C_f + C_r{}^xK_{eq}}{1 + C_f + C_r}$ (13)
14	$\dfrac{Q^*}{EA^*} = \dfrac{T^*_{max}B}{[Hx_{50}] + B}$ (14)
15	$\dfrac{k_2}{k_{cat}} = \dfrac{[Hx_{50}]}{K_{Hx}}$ (15)
16	${}^3H\ cpm = cpm_A - rcpm_B \quad {}^{14}C\ cpm = cpm_B(1 + r)$ (16)
17	$KIE_{V/K} = \dfrac{\log(1 - f)}{\log\left((1 - f)\frac{R_P}{R_0}\right)} = \dfrac{\log(1 - f)}{\log\left((1 - f)\left(\frac{R_s}{R_0}\right)\right)}$ (17)
18	$\%\ activity = Y_{min} + \dfrac{100 - Y_{min}}{\left(1 + \left(\frac{I}{IC_{50}}\right)^h\right)}$ (18)
19	$K_i = \dfrac{IC_{50}}{1 + \left(\frac{K_a}{A}\right)}$ (19)
20	$\dfrac{v_i}{v_o} = 1 - \dfrac{(E_t + I_t + appK_i) - \sqrt{(E_t + I_t + appK_i)^2 - 4E_tI_t}}{2E_t}$ (20)

(Invitrogen) and grown to an OD$_{600}$ of 0.6. The temperature was then decreased to 18 °C for 45 min. The culture was induced with 0.2% L-arabinose overnight and then harvested by centrifugation at 5,000 g for 20 min at 4 °C. All protein purification was performed at 4 °C unless otherwise stated. Cells were suspended in 20 mM Tris HCl, 5 mM imidazole, 500 mM NaCl, 1 mM DTT (pH 7.9)—cell suspension buffer, with DNase I, lysozyme (Sigma Millipore), and a protease inhibitor tablet (Roche) and stirred for 30 min. The cells were disrupted by sonication (two cycles pulsed for 15 s on and 15 s off at 30%

amplitude for 7 min and 30 s) and clarified by centrifugation at 20,000 g for 20 min. Ni-NTA agarose was prepared by washing the resin with 10 CV of cell suspension buffer, and the supernatant was added and incubated for 45 min on a rocker apparatus. The mixture was transferred to a Ni-NTA agarose column and subsequently washed with 10 CV of cell suspension buffer. A stepwise elution was performed using a gradient of 50–500 mM imidazole. Fractions of purified enzyme were analyzed by SDS-PAGE. The fractions containing PfHGXPRT (~26 kDa) were pooled and dialyzed in 50 mM KH$_2$PO$_4$ (pH 7.5), 5

mM imidazole, 150 mM KCl, 1 mM DTT, and 10% glycerol (v/v). Purified enzyme solutions were concentrated to ~300 μM, aliquoted, flash frozen in liquid nitrogen, and stored at −80 °C. *Hs*HGPRT was purified as previously described.[37]

A construct of *Sp*IMPDH containing a His$_6$ coding region with a downstream TEV protease cleavage site was designed and synthesized (GenScript), and the resulting DNA was incorporated into a pET-28b(+) plasmid, which contained a sequence encoding kanamycin resistance. The plasmid was overexpressed in *E. coli* BL21(DE3), and at an OD$_{600}$ of 0.6, protein expression was induced by the addition of 1 mM IPTG, followed by incubation overnight. All protein purification steps were performed at 4 °C. Cells were suspended in 50 mM KH$_2$PO$_4$ (pH 8.0), 500 mM KCl, 5 mM imidazole, 0.5 mM TCEP (pH 8.0), with the inclusion of protease inhibitor cocktail (Roche), a few milligrams of DNase I, and lysozyme. The solution was then stirred for 30 min. Cell lysis was achieved by two cycles of sonication pulsed for 15 s on and 15 s off at an amplitude of 30% for 7 min and 30 s, followed by centrifugation at 20,000 *g* for 20 min to remove insoluble fractions. The supernatant was added to a Ni-NTA slurry followed by incubation for 45 min with shaking. Protein was eluted from a Ni-NTA column using a stepwise gradient of imidazole from 50 to 250 mM. Fractions were analyzed by SDS-PAGE, and fractions containing *Sp*IMPDH (52.8 kDa) were pooled and dialyzed against 50 mM HEPES (pH 7.9), 100 mM KCl, and 20% (v/v) glycerol. The purified enzyme was aliquoted, flash frozen, and stored at −80 °C.

Kinetics and Inhibition Analysis of *Pf*HGXPRT and *Hs*HGPRT. The biosynthetic reaction of Hx incorporation into IMP, as catalyzed by *Pf*HGXPRT and *Hs*HGPRT, and analysis of inhibition were measured spectrophotometrically using an IMPDH-coupled assay (reaction R2). *Pf*HGXPRT was activated prior to the experiment by preincubating the enzyme with Hx, PRPP, and MgCl$_2$ for 30 min at 25 °C. The production of IMP as catalyzed by *Pf*HGXPRT and *Hs*HGPRT from Hx and PRPP was coupled to the formation of XMP, and the spectral change of NAD$^+$ to NADH was measured at 340 nm (reaction R2). All assays were performed in 50 mM HEPES (pH 7.4) containing 500 nM *Pf*HGXPRT, 3 μM *Sp*IMPDH, 1 mM Hx, 2 mM PRPP, 5 mM NAD$^+$, 10 mM MgCl$_2$, and 1 mM DTT. For inhibition assays, variable concentrations of inhibitors were added (0−100 μM). PPi (1.4 mM) was present in the reaction mixtures for inhibition analysis. Inhibitors were tested against both *Pf*HGXPRT and *Hs*HGPRT. Data were analyzed using GraphPad Prism 9 software by fitting to the Michaelis−Menten equation (eq 1) for steady-state calculations and to the Morrison equation (eq 20) for calculation of the inhibition constant (K_i)[54]

$$\text{PRPP} + \text{hypoxanthine} \xrightarrow[\text{Mg}^{2+}]{\text{HGXPRT}} \text{PPi} + \text{IMP}$$

$$\text{IMP} + \text{NAD}^+ \xrightarrow{\text{IMPDH}} \text{XMP} + \text{NADH} \qquad (\text{R2})$$

Data Analysis. *T. cruzi* steady-state kinetic and inhibition analysis was performed using GraphPad Prism 9.2 software, with the equations used in the analysis of all kinetic data listed in Table 1.

Initial velocity data obtained at variable concentrations of a single substrate A at single fixed concentration of a second substrate B were fit to eq 1 in which *v* is the initial velocity, E_t is the enzyme concentration, k_{cat} is the turnover number, *A* is the concentration of the variable substrate, and K_a is the apparent Michaelis constant.

Initial velocity data obtained at variable concentrations of a single substrate A and at several fixed concentrations of a second substrate B were fit to eq 2 in which K_{ia} and K_a are the respective dissociation and Michaelis constants of A, and K_b is the Michaelis constant of substrate B.

For inhibition studies in which double-reciprocal plots of inhibitor (I) *vs* variable substrate (A) conformed to apparent competitive, noncompetitive, or uncompetitive inhibition, respectively, initial velocity data (*v*) were fit globally to eqs 3−5 where E_t is the concentration of enzyme, k_{cat} and K_a are, respectively, the turnover number and the Michaelis constant for substrate A, and K_{is} and K_{ii} are, respectively, the apparent slope and intercept inhibition constants.

Ligand binding as determined by ITC provided values for the binding enthalpy ($\Delta H°$), the association constant (K_a), and the number of binding sites per monomer (*N*). The Gibbs free energy ($\Delta G°$) and the entropy ($−T\Delta S°$) of binding were calculated using the relationship described in eq 7, where *R* is the gas constant (1.987 cal K^{-1} mol^{-1}) and *T* is the temperature in Kelvin. K_d was calculated as the reciprocal of K_a.

The kinematic viscosity ($\eta_{kinematic}$) was calculated using the relationship described in eq 8, where *t* is the efflux time, and *K* is the viscometer constant. Dynamic viscosities ($\eta_{dynamic}$) were determined according to eq 9, where $\eta_{kinematic}$ is the kinematic viscosity and *d* is the density of the liquid. Equation 10 describes the relative viscosities, where η_0 is the viscosity when there is 0% viscosogen in the solution and η_x is the viscosity when there is *X* % of viscosogen in the solution.

Initial velocity data obtained at fixed concentrations of viscosogen were fit to eq 1 to afford the apparent kinetic parameters (k_{cat}, K_{PRPP}, and k_{cat}/K_{PRPP}) at each η_{rel} value. Viscosity data were plotted as the normalized kinetic parameter (*i.e.*, $[k_{cat}/(k_{cat})_\eta]$ or $[(k_{cat}/K_{PRPP})/(k_{cat}/K_{PRPP,\eta})]$) as a function of η_{rel} and fit to eq 11 where k/k_η is the normalized kinetic parameter, η_{rel} is the relative viscosity, and *m* is the slope of the line, which represents the dependence on viscosity on the normalized kinetic parameter.[43] Viscosity effects on k_{cat} were further applied to Kramer's model[55,56] and fit to eq 12, where $[k_{cat}/(k_{cat})_\eta]$ is the normalized k_{cat} value obtained during viscosity studies, η_{rel} is the relative viscosity, and *m* is the slope of the line.

The generalized equation for KIEs on *V/K* is depicted in eq 13, where *x* is the nature of the isotopic atom, $^xK_{eq}$ is the equilibrium isotope effect, $^xk_7$ is the intrinsic isotope effect on the isotope-sensitive step, and C_f and C_r are the forward and reverse commitment factors, respectively.

To determine the commitment of the binary TcC-PRPP* complex (EA*) to form labeled IMP* (Q*) at varying concentrations of Hx, the isotope trapping data were fit to the hyperbolic equation (eq 14) in which *B* is the fixed concentration of Hx in the pulse-chased solution and B_{50} is the concentration of Hx that traps half of the maximal fraction T_{max}*, which is the maximal amount of TcC-PRPP* (EA*) that is converted to IMP* (Q*).

The rate at which A* dissociates from EA* relative to k_{cat} (*i.e.*, k_2/k_{cat}, where k_{cat} represents all of the steps after the formation of the E-PRPP*-Hx complex—Figure S6) is described in eq 15,[49] where K_{Hx} is Michaelis constant of Hx determined at saturating concentrations of A (PRPP) during initial velocity studies and [Hx$_{50}$] is the trapping constant (*i.e.*, apparent K_m) from the reciprocal plot of $1/Q*$ *vs* $1/[Hx]$.[49]

For the determination of KIEs, the cpm in both the residual substrate and formed product were first measured. Radio-

Table 2. Apparent Kinetic Parameters of TcA and TcC

HGPRT	reaction	variable substrate	fixed substrate	apparent kinetic parameters[a]		
				K_m (μM)	k_{cat} (s^{-1})	k_{cat}/K_m ($\times$ 10^3 M^{-1} s^{-1})
TcA	GMP biosynthesis	Gua (5–200 μM)	PRPP (1 mM)	19 ± 1	32 ± 1	1700 ± 100
		PRPP (20–215 μM)	Gua (70 μM)	32 ± 5[b]	32[b]	1010[b]
	IMP biosynthesis	Hx (5–150 μM)	PRPP (1 mM)	13 ± 4	32 ± 1	2500 ± 700
		PRPP (20–215 μM)	Hx (60 μM)	31 ± 5[b]	23[b]	750[b]
	HPP-MP biosynthesis	HPP	PRPP (1 mM)	710 ± 130[c,d]	0.34 ± 0.03[c,d]	0.5 ± 0.1[c,d]
	XMP biosynthesis	Xan (50–500 μM)	PRPP (1 mM)	160 ± 40	0.005 ± 0.0006	0.03 ± 0.008
TcC	GMP biosynthesis	Gua (5–200 μM)	PRPP (1 mM)	14 ± 1	30 ± 1	2100 ± 200
		PRPP (6–200 μM)	Gua (100 μM)	33 ± 3	31 ± 1	930 ± 90
	IMP biosynthesis	Hx (5–150 μM)	PRPP (1 mM)	14 ± 2	35 ± 2	2500 ± 300
		PRPP (6–200 μM)	Hx (100 μM)	39 ± 2	24 ± 1	620 ± 40
	HPP-MP biosynthesis	HPP (50–750 μM)	PRPP (1 mM)	213 ± 35	2 ± 0.1	8 ± 2
	XMP biosynthesis	Xan (50–500 μM)	PRPP (1 mM)	150 ± 10	0.008 ± 0.0002	0.05 ± 0.005

[a]All assays were performed at 37 °C (pH 8.3) in the presence of 12 mM MgCl$_2$. Data were fit to eq 1 to afford apparent kinetic parameters. [b]Data obtained by Wenck et al.[34] [c]Data obtained by Allen et al.[33] [d]Kinetic parameters were determined with Lineweaver−Burk plots.

activities (cpm) corresponding to ^{3}H and ^{14}C were calculated by the relationship described in eq 16, where r is the ratio of cpm in channel A/channel B. KIEs were then calculated using eq 17, where f is the fraction of reaction, R_p is the ratio of heavy to light isotope in products, R_s is the ratio of heavy to light isotope in residual substrate, and R_0 is the initial ratio of heavy to light isotope in the substrate.[49]

The potency of *T. cruzi* HGPRT inhibitors was assessed for inhibitory activity with initial velocity data fit to eq 18 in which IC_{50} is the half-maximal inhibitory concentration, h is the Hill slope, Y_{min} is the minimum value of percentage activity, and I is the concentration of the inhibitor.[54] The intrinsic potency of TcC inhibitors (K_i) was determined using eq 19[54,57] in which IC_{50} is the half-maximal inhibitory concentration, A is the concentration of Hx, and K_a is the Michaelis constant for Hx, all assuming that uncompetitive inhibition exists for these inhibitors.

We employed an equation for inhibitors that are effective at concentrations equal to the enzyme to determine the inhibition constants (K_i) against *Pf*HGXPRT and *Hs*HGPRT (eq 20).[54,58] The residual activity (v_i/v_0) was plotted as a function of the concentration of the inhibitor (I). E_t is the concentration of total enzyme, v_0 and v_i are, respectively, the initial rates in the presence and absence of the inhibitor, I_t is the concentration of the inhibitor, and appK_i is the apparent inhibition constant.

■ RESULTS AND DISCUSSION

It has been demonstrated that in the absence of Mg^{2+}, no catalytic activity can be detected for PPRTs,[26] and the true HGPRT substrate is Mg·PRPP.[26] For this reason, throughout this section, when PRPP is cited as the substrate, it should be understood as the Mg·PRPP complex. Mg^{2+} was kept at a constant and noninhibitory concentration (12 mM) in all assays discussed (Figure S7). When PRPP concentrations were varied, the concentration of the Mg·PRPP complex formed is equivalent to the concentration of PRPP stated, as excess Mg^{2+} converts all PRPP to its Mg·PRPP complex.

Substrate Specificities of TcA and TcC as Determined by Steady-State Kinetics. Analysis of the genomic data of *T. cruzi* revealed two *hgprt* genes: the non-Esmeraldo-like TcCLB.509693.70 and the Esmeraldo-like TcCLB.506457.30. These encode two HGPRTs named herein, respectively, TcA and TcC that share >98% amino acid identity (Figure S1). Each enzyme was expressed and purified individually to determine

whether these isoforms are functionally distinct from each other, and the substrate specificity of both enzymes was further examined. Both TcC and TcA displayed an apparent homodimeric structure, which agrees with the previous crystallographic data of TcA[35] (Figure S8). Upon evaluation of the *in vitro* activity, TcA and TcC exhibited nearly identical apparent kinetic parameters for all three 6-oxopurine substrates (Table 2). Both TcA and TcC are highly efficient at catalyzing the formation of the *N*-ribosidic bond between PRPP and the 6-oxopurines Hx and Gua, with Hx being the preferred substrate ($k_{cat}/K_m \geq 1 \times 10^5$ M^{-1} s^{-1}; Figure S9). Surprisingly, both enzymes also catalyzed the formation of XMP from PRPP and Xan, albeit with significantly lower k_{cat}/K_m values (by a factor of 1×10^4) (Table 2 and Figure S9), suggesting that Xan is likely not a natural substrate of TcA and TcC and thus confirms their annotation as HGPRTs. Additionally, the 7-deaza, 8-aza analogue of Hx, allopurinol (HPP), was assessed as an alternative substrate of TcC. Our results indicated that HPP is a poor substrate of TcC, exhibiting a value of k_{cat}/K_m on the order of 10^3 M^{-1} s^{-1} (Table 2 and Figure S9). HPP was previously reported as a poor substrate for TcA, and the ribosylation of this purine analogue is believed to play a role in the toxicity of the compound in Trypanosomatids.[33,59]

Under the tested conditions, the apparent kinetic parameters of TcC were essentially identical to that previously reported for the TcA enzyme.[33−35] Therefore, both HGPRTs were found to be functionally identical, with essentially equal catalytic efficiencies for GMP, IMP, and XMP formation (Table 2). This finding is consistent with the divergence between the genes encoding TcA and TcC arising through random mutations that are not physiologically significant. Such an observation is of importance since genetic variance in *T. cruzi* is related to varied profiles of drug resistance in circulating strains, with HGPRT polymorphisms being correlated to drug susceptibility.[27] Therefore, identification and characterization of mutations that can impact the catalytic efficiency or kinetic mechanism of isoforms can be of use in studies of the emergence of drug resistance-related mutations and must be differentiated from polymorphic isoforms that show equivalent catalytic properties.

The TcA isoform has been previously characterized for its steady-state kinetics and *in vitro* screening of inhibitors.[60] Crystallography[35] and mutagenesis[34,35,60−62] studies were used to identify key residues involved in TcA catalysis. Data on the catalytic activity of TcC is, however, limited, so we focused the

Table 3. Initial Velocity Data of TcC and TcA

			kinetic parameters[a]					
enzyme	reaction	variable substrate	K_{IMP} (μM)	$K_{i,IMP}$ (μM)	k_{cat}/K_{IMP} ($\times 10^3$ M^{-1} s^{-1})	K_{PPi} (μM)	k_{cat}/K_{PPi} ($\times 10^3$ M^{-1} s^{-1})	k_{cat} (s^{-1})
TcA	IMP pyrophosphorolysis	PPi (15.6–500 μM)	16 ± 1^b	N.D.[c]	28^b	16 ± 2^b	29^b	0.46^b
TcC	IMP pyrophosphorolysis	IMP (31–1000 μM)	38 ± 5	490 ± 80	6.3 ± 0.4	11 ± 1	22 ± 1	0.24 ± 0.01

[a]All assays were performed at 37 °C (pH 8.3) in the presence of 12 mM MgCl$_2$. Data were globally fit to eq 2 to afford kinetic parameters. [b]Data for TcA obtained by Wenck *et al.*[34] [c]N.D., not determined.

Table 4. Product Inhibition Data of TcC

					apparent kinetic parameters[a]	
reaction	variable substrate	inhibitor	fixed substrate	inhibition pattern	K_m (μM)	K_{is} (μM)
IMP biosynthesis	PRPP (10–200 μM)	IMP (0–120 μM)	Hx (50 μM)	C[b]	35 ± 2	100 ± 10
GMP biosynthesis	PRPP (10–200 μM)	GMP (0–60 μM)	Gua (50 μM)	C[b]	22 ± 2	5 ± 1
IMP pyrophosphorolysis	IMP (12.5–500 μM)	PRPP (0–3 μM)	PPi (100 μM)	C[b]	110 ± 10	0.8 ± 0.1

[a]Assays were performed at 37 °C (pH 8.3) in the presence of 12 mM MgCl$_2$. Data were globally fit to eqs 3–5. All of the product inhibition data conformed to apparent competitive patterns, and fitting of the data to eq 3 afforded the apparent kinetic parameters. [b]C = competitive.
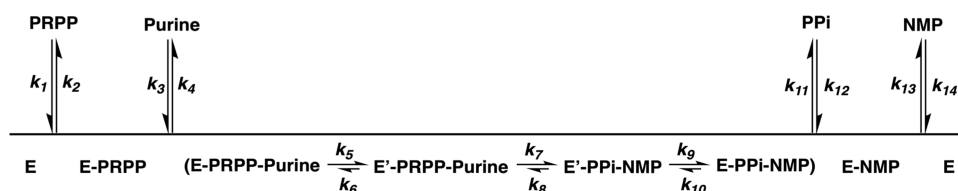
Figure 2. TcC operates *via* an ordered Bi Bi mechanism in which PRPP binds first followed by the 6-oxopurine (Hx or Gua). Once the E-PRPP-Purine complex forms, the flexible loop closes over the active site (k_5 step), converting the central complex to E'-PRPP-Purine. TcC catalysis converts E'-PRPP-Purine to E'-PPi-NMP for which $k_7 \gg k_8$, followed by opening of the flexible loop (k_9 step) to afford the E-PPi-NMP complex, which is followed by the ordered release of PPi and NMP (IMP or GMP).
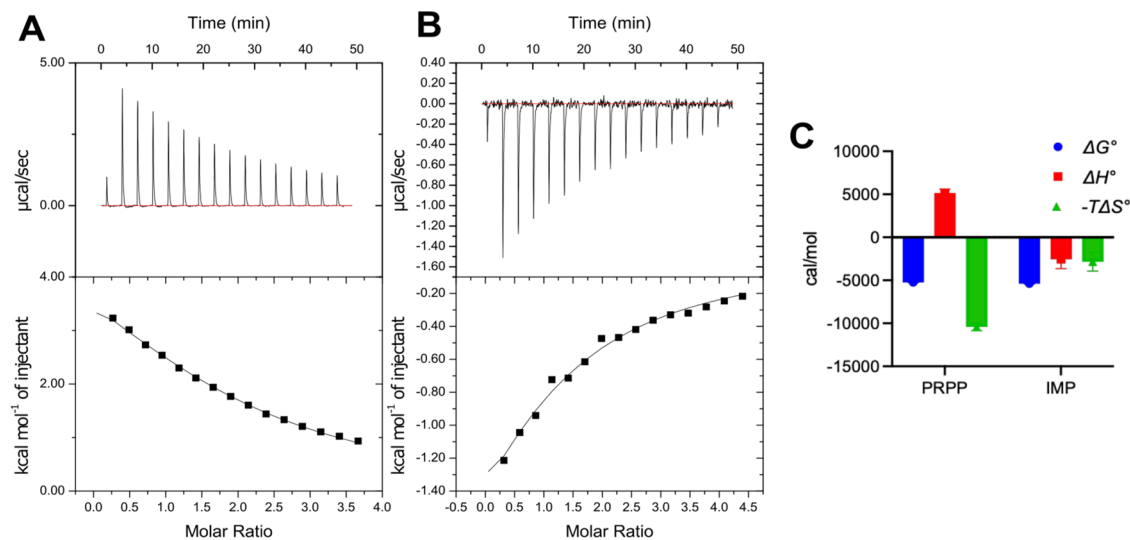
Figure 3. ITC binding assays of (A) PRPP and (B) IMP to free TcC enzyme, and (C) thermodynamic profiles of PRPP and IMP binding to free TcC enzyme.

remainder of our kinetic studies on the TcC isoform, focusing on the HGPRT mechanics of reaction and inhibition.

Initial Velocity Studies. TcC was further characterized to ascertain its kinetic mechanism. Initial velocity data of the reverse reaction (IMP *vs* PPi) when plotted in double-reciprocal form conformed to a pattern in which lines intersected to the left of the *y*-axis. This indicated that a sequential bi-substrate mechanism is operative for TcC (Table 3 and Figure S10). The kinetic constants for the reverse reaction matched closely with

that previously reported for the TcA enzyme.[34] The catalytic efficiencies (k_{cat}/K_{Hx} and k_{cat}/K_{Gua}) obtained for the biosynthetic reactions were essentially identical for the two isoforms (Table 2; 1.7×10^6 and 2.5×10^6 M^{-1} s^{-1} for TcA and 2.1×10^6 and 2.5×10^6 M^{-1} s^{-1} for TcC), and the values of k_{cat}/K_{IMP} for the reverse reaction were considerably smaller (Table 3; 2.8×10^4 and 6.3×10^3 M^{-1} s^{-1} for TcA and TcC, respectively). The 100-fold difference of k_{cat}/K_m values demonstrated that the biosynthetic reaction is highly favored.

Table 5. PRPP and IMP Binding Parameters to Apo TcC (Free Enzyme)

ligand	binding parameters[a]					
	$\Delta G°$ (cal mol^{-1})	$\Delta H°$ (cal mol^{-1})	$-T\Delta S°$ (cal mol^{-1})	K_a (M^{-1})	K_d (μM)	N
PRPP	-5247 ± 5	5160 ± 450	$-10,410 \pm 450$	7070 ± 60	142 ± 1	1.2 ± 0.2
IMP	-5380 ± 40	-2540 ± 1090	-2840 ± 1089	8880 ± 60	113 ± 1	1.0 ± 0.2

[a]All binding assays were performed at 25 °C (pH 8.0). Data were fit to the one-set-of-sites model and to eq 7 to afford binding parameters. Uncertainties represent the standard deviation between replicates. The reference power was set to 11 μcal s^{-1} and 1 cal = 4.18 J.
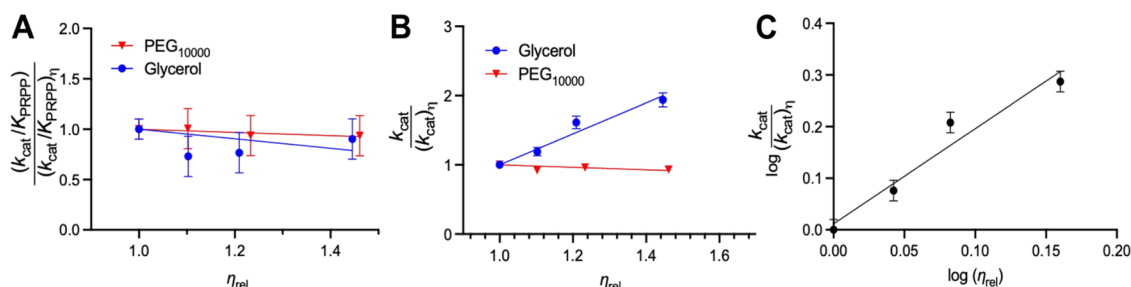
Figure 4. (A) Viscosity effects on k_{cat}/K_{PRPP} of TcC. In the presence of glycerol (blue), k_{cat}/K_{PRPP} increased, thus exhibiting an inverse effect. Data were fit to eq 11, which provided a slope of -0.5 ± 0.3. The macroviscosogen control (PEG$_{10,000}$) is shown in red. (B) Viscosity effects on k_{cat} of TcC. Increasing levels of glycerol (blue) decreased the apparent k_{cat} of TcC, and fitting of the data for the plot of $k_{cat}/(k_{cat})_\eta$ vs η_{rel} to eq 11 resulted in a slope of 2.2 ± 0.2. The macroviscosogen control (PEG$_{10,000}$) is shown in red. (C) TcC viscosity effects on k_{cat} fit to eq 12, providing a slope of 1.8 ± 0.3.

This observation supports the assumption that the primary cellular role of the HGPRTs is scavenging Hx and Gua from hosts and their incorporation into nucleotides and nucleic acids *via* the purine salvage pathway. A greater preference for the forward reaction can be expected for obligatory purine auxotrophs.

Product Inhibition. Product inhibition studies were performed to provide information on the kinetic mechanism. Product inhibition of the forward reaction with IMP or GMP *vs* variable concentrations of PRPP provided apparent competitive patterns (Figure S11). Additionally, product inhibition of the reverse reaction with PRPP *vs* variable concentrations of IMP also conformed to a competitive pattern (Table 4 and Figure S11), indicating that PRPP and IMP (or GMP) bind to the same enzyme form. Notably, the apparent K_{PRPP} in the presence of saturating Hx is nearly identical to the apparent K_{PRPP} in the presence of saturating Gua (Table 2), corroborating the finding that PRPP is the first substrate to bind to the TcC enzyme. Furthermore, the apparent competitive patterns for IMP (or GMP) *vs* PRPP in both the forward and reverse reactions suggested an ordered kinetic mechanism for TcC where the phosphoribosyl donor, PRPP, binds to free enzyme, followed by the second substrate, 6-oxopurine (Hx or Gua). After catalysis, PPi is the first product to dissociate from the enzyme–product complex, followed by NMP (IMP or GMP) (Figure 2). The Haldane equation (eq 6) describes the relationship between the equilibrium constant (K_{eq}) and the kinetic constants ($V_{max,f}$, $V_{max,r}$, K_{iq}, K_{ia}, K_p, and K_b).[63] When the respective K_m ($K_{m,PRPP}$ = 39 ± 2 and $K_{m,Hx} = 14 \pm 2$—Table 2; $K_{m,PPi} = 11 \pm 1$ and $K_{m,IMP}$ = 38 ± 5—Table 3), K_{is} ($K_{is,PRPP} = 0.8 \pm 0.1$ and $K_{is,IMP} = 100 \pm 1$—Table 4), and V_{max} ($V_{max,f} = 82 \pm 3$ and $V_{max,r} = 0.32 \pm 0.01$—Figure S9) values of TcC IMP biosynthesis are substituted in the expression for an ordered Bi Bi mechanism (eq 6), $K_{eq} = 25,000 \pm 6,000$, further demonstrating that the biosynthetic reaction is highly favored.

Ligand Binding Measured by ITC Binding Assays. ITC binding assays were performed with PRPP, Hx, PPi, and IMP to confirm the order of substrate binding and product release. The binding assays showed that both PRPP (in the presence of

Mg^{2+}) and IMP bind to free TcC enzyme (Figure 3A,B), which agrees with the product inhibition data as PRPP *vs* NMP provided an apparent competitive pattern (Figure S11). ITC data for PRPP and IMP binding were fit to the one-set-of-sites model[42] (Table 5). The thermodynamic signatures for binding of PRPP and IMP suggested that binding of PRPP is enthalpically unfavorable and is largely driven by hydrophobic forces and/or solvent rearrangement, while IMP binding resulted in a small favorable contribution from both enthalpy ($\Delta H°$) and entropy ($-T\Delta S°$) (Figure 3C). Due to enthalpy–entropy compensations,[64] the thermodynamic profile for IMP binding suggests an inhibitor that mimics the structure of IMP could provide high specificity and tight binding affinity. The near-unity value for the number of binding sites (N) for both PRPP and IMP indicated that there is one ligand molecule bound to each subunit (Table 5). Conversely, binding of Hx and PPi to free TcC enzyme could not be detected even when ligand concentrations were 500- and 900-fold higher than their respective K_m values (Figure S12). Binding of Gua to free TcC enzyme could not be evaluated by ITC studies due to the limited solubility of the nucleobase in the assay conditions. The apparent competitive pattern of GMP *vs* PRPP in the product inhibition studies suggested that GMP can also bind to free TcC enzyme (Figure S11), and since Hx and Gua present similar structures and apparent kinetic parameters, it is assumed that TcC would conform to the same kinetic mechanism regardless of whether Hx or Gua is used as the substrate. The ITC binding data corroborated the ordered Bi Bi kinetic mechanism proposed for TcC (Figure 2). Most PPRTs, including TcA, follow a highly conserved ordered-sequential kinetic mechanism in which the binding of PRPP precedes that of the nucleobases.[34,65−67] The previous characterization of the ordered-sequential kinetic mechanism of TcA also proposes the formation of a dead-end E-Hx-PPi complex when both ligands are present at high concentrations, as suggested by limited proteolysis studies, and advocates the design of bi-substrate analogues as potential high-potency inhibitors of TcA,[34] which is in agreement with the ITC results (Figure 3).

Viscosity Effects on k_{cat}/K_{PRPP} and k_{cat}. Microviscosogens, such as glycerol, increase the microviscosity of the solution, affecting the rates of diffusional steps, including the binding and desorption of small ligands to enzymes, and thus providing information on the rate-limiting step(s) of catalysis.[68−70] Macroviscosogens, such as $PEG_{10,000}$, only increase the macroviscosity of the solution, and therefore diffusional steps are not affected. Both macroscopic and microscopic viscosogens were used during viscosity studies to confirm that an observed effect was due to diffusional processes rather than a crowding effect.[43] We investigated the effects of viscosity on the apparent k_{cat} and the apparent k_{cat}/K_{PRPP} of TcC to determine whether substrate binding and/or product release contribute to the rate-limiting step(s) during catalysis. Initial velocity data of mixtures contained increased fixed levels of viscosogen (0, 4, 8, and 12% v/v glycerol or 0, 0.5, 1, 2% w/v $PEG_{10,000}$), variable concentrations of PRPP (6−200 μM), and 20 μM Hx. Initial velocity data were fit to eq 1, which provided the viscosity-dependent values of k_{cat} and k_{cat}/K_{PRPP}. While the apparent k_{cat}/K_{PRPP} increased slightly in the presence of glycerol, the apparent k_{cat} decreased proportionally with increasing concentrations of glycerol. Both the apparent k_{cat}/K_{PRPP} and k_{cat} showed relatively little changes in the presence of $PEG_{10,000}$. Normalized kinetic values—$(k_{cat}/K_{PRPP})/(k_{cat}/K_{PRPP})_\eta$ or $k_{cat}/(k_{cat})_\eta$—were then plotted vs η_{rel} and fit to eq 11.[43] Increasing fixed levels of glycerol had a small negative effect on k_{cat}/K_{PRPP} (slope = -0.5 ± 0.3—Figure 4A), which suggested that the effect of glycerol on the enzyme-catalyzed reaction is not associated with the diffusion of either enzyme or PRPP.[43] Furthermore, the presence of an inverse linear effect on k_{cat}/K_{PRPP} has previously been shown to be associated with an isomerization mechanism for the enzyme that accompanies the binding of substrates to the enzyme.[43,56] In contrast, normalized values of $k_{cat}/(k_{cat})_\eta$ vs η_{rel} were plotted, which exhibited a linear pattern (Figure 4B) with a slope of 2.2 ± 0.2. A slope greater than 1 on the $k_{cat}/(k_{cat})_\eta$ vs η_{rel} plot indicates that the observed effect is not strictly associated with desorption of products, suggesting that a post-chemistry event, such as a conformational change of the enzyme could be rate limiting, as the microviscosogen will restrict the movement of either large protein domains or protein loops that are involved as part of catalysis or to enable product release from a closed active site.[43,56] Raber, Freeman, and Townsend[56] showed that the opening of active-site loops in *Streptomyces clavuligerus* β-lactam synthetase catalysis (*i.e.*, the rate-limiting step) was restricted by the friction imposed by high relative microviscosities using Kramer's model[55,56] (eq 12). Kramer's theory explains the unimolecular rate dependence on solvent viscosity and illustrates that rates are inversely proportional to friction for diffusive barrier crossings.[56] TcC microviscosogen effects on k_{cat} were applied to Kramer's theory (eq 12) and at increasing $\log(\eta_{rel})$, the $\log(k_{cat}/(k_{cat})_\eta)$ values increased proportionally with a slope of 1.8 ± 0.3 (Figure 4C), which is nearly identical to the results reported for β-lactam synthetase (slope = 1.7 ± 0.08).[56] These results suggested that increasing solvent viscosity increased solvent friction and likely increased the internal protein friction, leading to decreased rates of structural rearrangements necessary for TcC catalysis.

A distinctive feature among PPRT structures is a long flexible loop closely associated with the active site, termed the "catalytic" or "flexible" loop (loop II, Figures S1, S13, and S15).[71,72] After both substrates are bound, the flexible loop closes over the active site to facilitate enzyme catalysis (Figure S13, bottom panel). The flexible loop has been implicated in substrate binding and

product release of previously characterized PPRTs, and its conformational change has been determined to be the rate-limiting step in their catalysis.[71,73,74] The flexible loop is also proposed to be essential for transition-state (TS) stabilization during phosphoribosyl transfer, and to shield the TS from the bulk solvent.[35,71,72,74,75] In the case of *T. cruzi* HGPRTs, the flexible loop has previously been implicated to play a role in both TS stabilization and the release of product PPi.[35,72,75]

In a previous study on TcA, seven residues on the flexible loop (residues 82−88, YGEGLTS—Figure S1) were deleted, and a comparison of the steady-state parameters revealed a dramatic decrease in k_{cat} in both the forward (380- and 840-fold reductions for IMP and GMP formation, respectively) and reverse (470-fold for IMP pyrophosphorolysis) reactions, highlighting its importance in enzyme catalysis.[75] Furthermore, the authors also reported a 6-fold increase in K_{PPi}, which is consistent with the flexible loop having a role in catalysis by properly coordinating the pyrophosphate portion of substrate PRPP, and PPi release from the active site.[75] A previously reported crystal structure of TcA revealed that when the flexible loop is closed, it makes four hydrogen-bonding interactions with oxygen atoms of PPi and metal-coordinated water molecules, thus supporting the observation that the flexible loop is involved in the coordination of both free PPi and its moiety in PRPP.[35]

Our findings that increasing levels of microviscosogen lower k_{cat} for TcC are consistent with a flexible-loop motion concomitant with or preceding the release of the first product PPi, while the viscosity effects on k_{cat}/K_{PRPP} may represent a mechanistic isomerization step in TcC catalysis, as previously described for *Mycobacterium tuberculosis* orotate phosphoribosyltransferase and in *S. clavuligerus* β-lactam synthetase.[56,73] The rate-limiting step of TcA catalysis has not been determined; therefore, the results presented for TcC indicate that the rate-limiting step of *T. cruzi* HGPRT catalysis is the opening of the flexible active-site loop and concomitant release of the first product, PPi. Our findings are in accord with that described for *Hs*HGPRT, where a post-chemistry event is the rate-limiting step of catalysis.[65] Xu *et al.* demonstrated that both the products (PPi and IMP) are released from the enzyme at least an order-of-magnitude slower than the chemical step (phosphoribosyl transfer) and that the rate of IMP release was about half that of PPi.[65] The viscosity data for TcC suggests that, like *Hs*HGPRT, a post-chemistry event largely comprises the rate-limiting step(s) and that the release of products follows structural rearrangement of the enzyme (Figure 2).

Isotope Partitioning Studies and Commitment to Catalysis. One must obtain a value for the commitment factor(s) of k_{cat}/K_{PRPP} to solve the intrinsic KIEs for evaluation of the TS of the chemical mechanism of *T. cruzi* HGPRT. For the ordered Bi Bi kinetic mechanism of TcC (Figure 2), the forward commitment factor (C_f) is defined as $C_f = \frac{k_7}{k_6}\left(1 + \frac{k_5}{k_4}\left(1 + \frac{k_3 B}{k_2}\right)\right)$, where B is the concentration of Hx[76] and describes the net partitioning of the E-PRPP complex proceeding to E-PRPP-Purine and then the products, vs the release of PRPP from the E-PRPP complex. The relationship between C_f and the concentration of Hx is such that increasing fixed concentrations of Hx raise the apparent value of C_f.[77] Regardless of whether the bound PRPP contains a heavy or light atom at the anomeric carbon, it becomes trapped in the TcC-PRPP-Hx complex at high concentrations of Hx, resulting in the suppression of the value of the intrinsic tritium isotope effect $(^{\alpha\text{-}T}k)$ on the experimental values of $^{\alpha\text{-}T}(V/K_{PRPP})$.

We employed the isotope partitioning method of Rose[47,48] to measure the forward commitment to catalysis of PRPP. Here, a preformed solution of enzyme and radiolabeled PRPP (PRPP*, pulse solution) is rapidly mixed with a panel of chase solutions containing a large excess of unlabeled PRPP and variable concentrations of Hx, followed immediately by quenching of the reaction to ensure few turnover events. Data were fit to eq 15 and a double-reciprocal plot of [E-PRPP*]/[IMP*] vs 1/[Hx] showed the expected linear plot in which the y-intercept provided the maximal value of [E-PRPP*]/[IMP*], $T_{max}* = 0.98 \pm 0.01$, and the slope, $[Hx]_{50}/T_{max}* = 2.0 \pm 0.2\,\mu M$ (Figure 5). Accordingly, at the y-intercept of the plot in Figure 5, [Hx] is
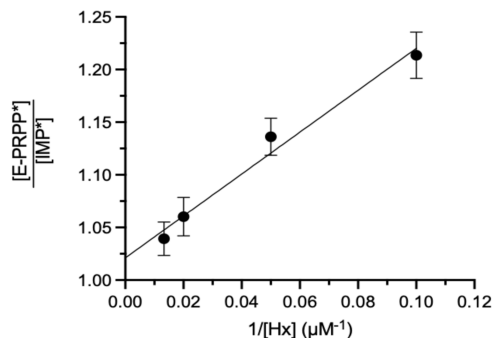
Figure 5. Isotope partitioning of E-PRPP* (EA*) to IMP* (Q*) increased with increasing concentrations of Hx to a limiting value (Hx $\Rightarrow \infty$) for IMP*/E-PRPP* (Q*/EA*) of 0.98 ± 0.01.

effectively infinite at which virtually all of the E-PRPP*-Hx complex is converted to product IMP* as would be expected for an ordered Bi Bi kinetic mechanism and provides additional corroboration of the kinetic mechanism in steady-state kinetic studies as determined above (Figure 2). Under these conditions, the calculated value of $[Hx]_{50}/K_{Hx} = k_2/k_{cat} = 0.14 \pm 0.02$ (eq 15),[49] indicating that PRPP is a "sticky" substrate, that is, its rate constant of desorption from the binary E-PRPP complex (k_2) is much lower than the rate constant of the chemical step (k_{cat}).[49] The ratio $k_{cat}/k_2 = 7 \pm 1$; therefore, it can be assumed that the value for C_f is significantly greater than 1, considering the mechanism described in Figure 2.

Kinetic Isotope Effects (KIEs). Both S_N1- and S_N2-type reactions have been proposed as possible mechanisms for *T.*

cruzi HGPRTs.[35,72] An associative S_N2 mechanism would proceed *via* nucleophilic attack from the 6-oxopurine at the N9 position on the anomeric carbon of PRPP, concomitant with PPi release. A S_N1 mechanism would involve formation of a discrete, cationic oxocarbenium TS (Figure 6A), which requires isolation from or a lifetime shorter than diffusional capture by the bulk solvent to prevent nonproductive PRPP hydrolysis.[72] Since the flexible loop closes over the active site upon substrate binding, an S_N1 mechanism is reasonable for the *T. cruzi* HGPRTs as it would prevent bulk solvent from entering the active site during catalysis. The assessment of α-secondary tritium isotope effects has been used in mechanistic studies to elucidate the TS structure.[77,78]

We therefore sought to ascertain the KIEs of radiolabeled PRPP in which the anomeric proton and carbon were substituted with heavy, radioactive atoms, $[1\text{-}^3\text{H}]$PRPP and $[1\text{-}^{14}\text{C}]$PRPP.[45] The remote radiolabeled samples of PRPP ($[5\text{-}^3\text{H}]$PRPP and $[5\text{-}^{14}\text{C}]$PRPP) were synthesized containing ^1H and ^{12}C at the anomeric carbon (Figure 6B). The heavy isotopes at C5 expressed a negligible isotope effect, and so the remote labels of ^3H and ^{14}C atoms at C5 provided a means to measure substrate turnover by radiometry when PRPP contained ^1H and ^{12}C at the anomeric carbon, respectively.[45] Values of the α-secondary tritium isotope effects $^{\alpha\text{-T}}(V/K_{PRPP})$ and primary carbon isotope effects $^{14}(V/K_{PRPP})$ on the anomeric carbon were obtained by measurement of the changes in the ratios of $^3\text{H}/^{14}\text{C}$ of purified, post-reaction samples of the remaining substrate PRPP and product IMP (Figure 6 and Table 6). All experimental KIEs were either equal to or only slightly different from unity. The KIEs obtained by analysis of either the purified residual substrates or products agreed, despite their modest values, suggesting that these values represent accurate isotope effects.

Values of $^{\alpha\text{-T}}(V/K_{PRPP})$ equaled 1.008 ± 0.001 and 1.000 ± 0.004 at fixed concentrations of 10 and 50 μM Hx, respectively, which are the approximate K_m and $5 \times K_m$ values of Hx. This observed "unmasking" of the small KIE of $^{\alpha\text{-T}}(V/K_{PRPP}) = 1.008$ at 10 μM Hx from the unity value found at 50 μM Hx is consistent with an ordered Bi Bi mechanism for TcC.[49] This is because increasing concentrations of Hx, the obligate second substrate of TcC, will increasingly suppress the values of $^{\alpha\text{-T}}(V/K_{PRPP})$ as it traps E-PRPP in the E-PRPP-Hx complex such that the enzyme cannot favor catalysis of $[1\text{-}^1\text{H}]$PRPP over that of
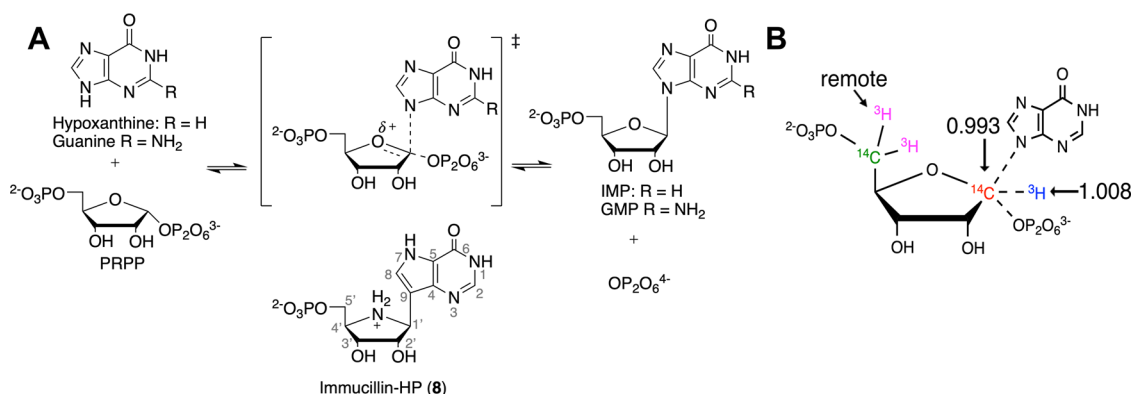
Figure 6. (A) *Pf*HGXPRT S_N1-like reaction mechanism, showing the oxocarbenium TS structure.[45,79] *Pf*HGXPRT TSAI Immucillin-HP (**8**) is compared to the proposed S_N1-like TS. The iminoribitol ring of **8** (when protonated) mimics the positive charge in the oxocarbenium TS. (B) Experimental KIEs on TcC with radiolabeled PRPP. The remote labels (5-^{14}C and 5-^{3}H) are shown in pink and green, respectively; the anomeric proton label (1-^{3}H) is shown in blue, and the anomeric carbon label (1-^{14}C) is shown in red.

Table 6. Measured KIEs of $^{\alpha\text{-T}}(V/K_{PRPP})$ and $^{14}(V/K_{PRPP})$ of TcC

heavy PRPP[a]	light PRPP[b]	KIE measurement (substrate, product)	purine	f^c	$^{\alpha\text{-T}}(V/K_{PRPP})$
1-^{3}H	5-^{14}C	[1-^{3}H]PRPP, [1′-^{3}H]IMP	Hx, 10 μM	0.64−0.70	1.007 ± 0.001, 1.008 ± 0.001
		[1-^{3}H]PRPP, [1′-^{3}H]IMP	Hx, 50 μM	0.58−0.61	1.000 ± 0.004, 1.000 ± 0.004
		[1-^{3}H]PRPP, [1′-^{3}H]IMP	HPP, 190 μM	0.35−0.61	1.00 ± 0.03, 1.00 ± 0.01
heavy PRPP[a]	light PRPP[b]	KIE measurement (substrate, product)	purine	f^c	$^{14}(V/K_{PRPP})$
1-^{14}C	5-^{3}H	[1-^{14}C]PRPP, [1′-^{14}C]IMP	Hx, 50 μM	0.59−0.61	0.993 ± 0.001, 0.994 ± 0.001
		[1-^{14}C]PRPP, [1′-^{14}C]IMP	HPP, 190 μM	0.78−0.80	1.005 ± 0.003, 1.005 ± 0.001

[a]Assays were performed at RT (pH = 7.4). KIEs were determined by isolation and quantitation of both radiolabeled substrates and products. [b]The binding isotope effects for the remote-labeled [5-^{3}H] or [5-^{14}C]PRPP have been shown to be negligible.[45] Data were fitted to eqs 16 and 17 to afford the values for the KIEs on V/K_{PRPP}. [c]f is the fraction of reaction.

[1-^{3}H]PRPP. This data is consistent with the results from the isotope partitioning study; that is, Hx traps PRPP in the binary E-PRPP complex.
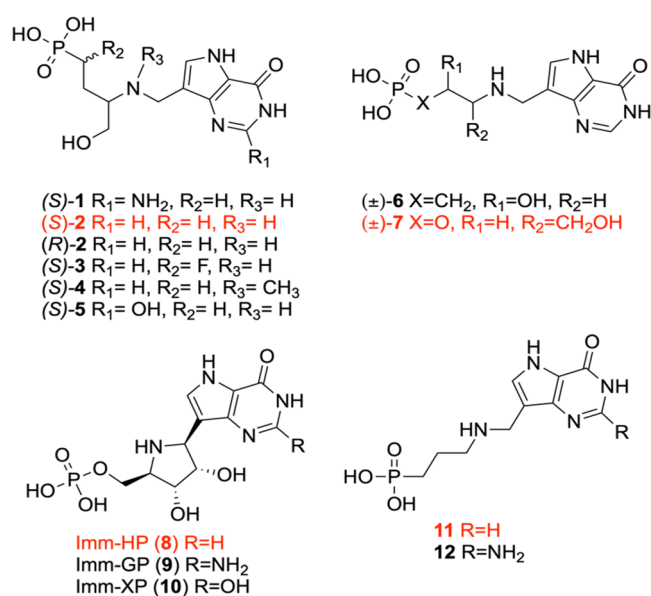
We also evaluated KIEs using the poor TcC substrate HPP for which chemical steps could be fully rate-limiting ($k_7 \ll k_3$B, Figure S6), potentially resulting in a small C_f and unmasking of the intrinsic KIEs on the k_7 step (Figure 2). The value of k_{cat}/K_{HPP} is roughly 1×10^3-fold lower than that of k_{cat}/K_{Hx} and k_{cat}/K_{Gua} (Table 2). Interestingly, the value of $^{\alpha\text{-T}}(V/K_{PRPP})$ measured at 190 μM HPP ($0.9 \times K_{HPP}$) was near unity (Table 6), as was also observed with Hx (at K_{Hx} and $5 \times K_{Hx}$). The primary ^{14}C KIE with Hx as substrate was slightly inverse, $14(V/K_{PRPP}) = 0.994 \pm 0.001$. Using HPP as the substrate, $^{14}(V/K_{PRPP}) = 1.005$ (Table 6). The lack of significant isotope effects for the poor substrate HPP corroborates a nonchemical step as rate limiting to catalysis, preventing an interpretation of the measured KIEs in terms of the TS structure. These results agree with what we observed during the analysis of viscosity effects on the apparent k_{cat} and k_{cat}/K_{PRPP}, again indicating that a post-chemistry physical change, presumably a conformational change, is the rate-limiting step in TcC catalysis and not chemistry. Accordingly, since a post-chemical step, such as opening of the active site to facilitate product desorption, is rate limiting, the catalytic mechanism of TcC (Figure 2) is incompatible with determination of intrinsic KIEs to solve the TS structure.[49]

As the use of the poor substrate HPP, with a presumably smaller value of C_f failed to unmask the intrinsic KIE ($^*k_7$), the lack of expression of the intrinsic KIE on the measured values of $^{\alpha\text{-T}}(V/K_{PRPP})$ and $^{14}(V/K_{PRPP})$ is likely due to a large value of the reverse commitment factor, C_r, where $C_r = \frac{k_8}{k_9}\left(1 + \frac{k_{10}}{k_{11}}\right)$, according to the mechanism proposed in Figure 2. Since we have shown that the opening of the active-site loop (k_9 step) is rate limiting for the reaction, C_r must also be large, and so $^{\alpha\text{-T}}(V/K_{PRPP}) = {}^{\alpha\text{-T}}K_{eq\,7}$, and accordingly, $^{14}(V/K_{PRPP}) = {}^{14}K_{eq\,7}$. The forward and reverse catalytic steps apparently come to equilibrium, and the measured KIEs are indeed equilibrium isotope effects, as previously observed with the malarial and human purine nucleoside phosphorylase enzymes (PfPNP and HsPNP).[72] If this is the case, we cannot extract intrinsic KIE values for either isotope. These small equilibrium isotope effects ($^{\alpha\text{-T}}K_{eq\,7} = 1.000$ and $^{14}K_{eq\,7} = 0.994$, at 50 μM Hx) are in accord with the fractionation of heavy and light isotopes between PRPP and IMP, both of which have sp^3 hybridization at the anomeric carbon.[80,81] In addition, the measured isotope effects (Table 6), which may represent equilibrium values, are similar to those reported for PfPNP,[80] HsPNP,[80] PfHGXPRT,[45] and HsHGPRT.[78] Consequently, purine nucleotide analogues such as Immucillin-HP (8), a TSAI of PfHGXPRT (Figure 6A),

which contain structures resembling the oxocarbenium ion of the putative TS of HGPRT catalysis, may serve as potent inhibitors of PPRTs.[53,82]

Potent inhibitors of *T. cruzi* HGPRTs. TS analysis of PfHGXPRT indicated that NMP biosynthesis likely proceeds *via* a S_N1-like reaction mechanism.[45] The PNP inhibitors known as Immucillins, which contain structural mimics of the ribooxacarbenium ion in the S_N1 reaction mechanism, are exceptionally potent inhibitors of PfPNP and PfHGXPRT.[36,37,52,83,84] Despite the known high variability on the primary sequence of PPRTs,[26] the active sites of PfHGXPRT and *T. cruzi* HGPRTs are extensively conserved, including all PfHGXPRT amino acids determined to interact with TSAIs (Figure S13). Considering the structural conservation between PfHGXPRT and *T. cruzi* HGPRTs and the putative S_N1-like reaction mechanism of both enzymes, we evaluated a subset of Immucillins that are TSAIs of PfHGXPRT as potential TcC inhibitors (Chart 1).

We initially performed concentration−response curves with each of the compounds to determine their apparent potencies (IC_{50}; Figure S14) at apparent saturating concentrations of PRPP (1 mM) and Hx (120 μM). All tested inhibitors displayed

Chart 1. TSAIs of PfHGXPRT Evaluated as Inhibitors of *T. cruzi* HGPRTs[a]

(S)-**1** R$_1$= NH$_2$, R$_2$=H, R$_3$= H
(S)-**2** R$_1$= H, R$_2$= H, R$_3$= H
(R)-**2** R$_1$= H, R$_2$= H, R$_3$= H
(S)-**3** R$_1$= H, R$_2$= F, R$_3$= H
(S)-**4** R$_1$= H, R$_2$= H, R$_3$= CH$_3$
(S)-**5** R$_1$= OH, R$_2$= H, R$_3$= H

(±)-**6** X=CH$_2$, R$_1$=OH, R$_2$=H
(±)-**7** X=O, R$_1$=H, R$_2$=CH$_2$OH

Imm-HP (**8**) R=H
Imm-GP (**9**) R=NH$_2$
Imm-XP (**10**) R=OH

11 R=H
12 R=NH$_2$

[a]A representative compound from each group (red) was further characterized for its mode of inhibition against TcC. The structure of each inhibitor is also shown in Figure S14.

Hill slopes of 0.60−1.66 in which values <0.8 and >1.2 may indicate possible cooperativity (negative and positive, respectively) between TcC subunits for the binding of some classes of inhibitors. A Hill slope that differs from unity has been previously described for Immucillins that are TS mimics of HsHGPRT.[83] No cooperativity was observed for TcC initial velocity assays (Tables 2−4 and Figures S9 and S10), however; it is not unusual for an enzyme to display cooperativity of inhibitor binding, and not that of the substrate(s).[54,63] HGPRTs contain a highly conserved cis-peptide bond between residues Leu51 and Lys52 on active-site loop I[72] (Figure S1). The side chain of Lys52 projects into the dimer interface and forms a 2.7 Å hydrogen bond to the carbonyl group of Met74 on strand β3 of the adjacent subunit (Figure S15).[35] Thus, a component of one of the active-site loops of HGPRT (loop I) is directly linked to the adjacent subunit, providing a possible mechanism for cooperativity between the two active sites.[72] In short, the flexible loop (loop II) closure over the active site after the binding of substrates could trigger conformational changes on loop I that impact the active-site affinity on the adjacent subunit. Isomerization of the Leu−Lys peptide bond from trans to cis upon substrate(s) binding has been linked to PfHGXPRT transition from inactive dimers to active tetramers, along with a significant increase in PRPP binding affinity,[66] and has been identified as the trigger to extensive conformational changes observed in HsHGPRT upon substrate(s) binding.[85]

The mode of inhibition of a representative compound from each of the four subgroups of Immucillins (Chart 1, red) was determined at variable concentrations of Hx (30−180 μM) and at apparent saturating conditions of PRPP (1 mM). At increasing concentrations of Hx, the apparent IC_{50} values decreased curvilinearly, which is indicative of uncompetitive inhibition (Figure S16). Such a pattern of uncompetitive inhibition lays additional support to the ordered Bi Bi mechanism proposed for T. cruzi HGPRTs. Uncompetitive inhibition was further demonstrated in patterns of inhibitor vs Hx at 1 mM PRPP with optimal fitting of the initial velocity data to eq 5, with apparently parallel double-reciprocal plots as shown in Figure S17 and Table S1. T. cruzi HGPRT K_i values for all inhibitors (Table 7) were determined according to the relationship described by Cheng and Prusoff for uncompetitive inhibition (eq 19).[57] PfHGXPRT and HsHGPRT K_i values were determined by fitting the inhibition data to eq 20.[54]

Unsurprisingly, all of the Hx-based ((S)-2, (R)-2, 3, 4, 6, 7, 8, and 11) and Gua-based (1, 9, and 12) inhibitors have higher potency against T. cruzi HGPRT than the Xan-based compounds (5 and 10) (Chart 1 and Table 7). All Hx-based and Gua-based inhibitors bind tightly, with K_i values at least 25-fold lower than K_{IMP} and K_{PRPP}, indicating that they are potent inhibitors of TcC. Hx-based 8 and Gua-based 9 are purine monophosphate analogues (Immucillins[53,86]) of IMP and GMP respectively, where the ether oxygen on the sugar is replaced with an NH group, and the nitrogen at position 9 on the 6-oxopurine is replaced with a carbon (Chart 1 and Figure 6A). The two-atom replacement in inhibitor 8 in comparison to substrate IMP comprises a 200-fold increase in binding affinity ($K_i/K_{IMP} \sim 1 \times 10^{-3}$). The tight binding of 8 to the enzyme is likely due to replacement of the ribose oxygen with a protonated nitrogen atom, which was designed to mimic the putative oxocarbenium cation of the TS (Figure 6A), and supports our previously observations that TcC likely follows an S_N1-like mechanism.

Table 7. Immucillin Inhibitors of T. cruzi HGPRT, HsHGPRT, and PfHGXPRT

inhibitor	T. cruzi HGPRT[a] (appK_i nM)	HsHGPRT[b] (appK_i nM)	SI[c]	PfHGXPRT[b] (appK_i nM)
1	15 ± 2	20 ± 0.3	1.3	N.D.[d]
(S)-2	13 ± 2	380 ± 40	29	0.65 ± 0.04
(R)-2	480 ± 30	16,000 ± 1000	33	23 ± 2
3	26 ± 2	420 ± 10	16	1.2 ± 0.1
4	1440 ± 30	4600 ± 70	3.2	108 ± 30
5	13,400 ± 900	>100,000	>7.5	8000 ± 500
6	170 ± 20	>10,000	>59	9.1 ± 0.1
7	1090 ± 260	>10,000	>9	N.D.
8	180 ± 30	1.8 ± 0.8	0.01	1 ± 0.3
9	1160 ± 390	4.6 ± 0.7	0.004	14 ± 2
10	36,720 ± 670	>100,000	>2.7	>100,000
11	710 ± 170	1350 ± 30	1.9	61 ± 3
12	3630 ± 320	1000 ± 5	0.3	107 ± 6

[a]T. cruzi HGPRT assays were performed at 37 °C (pH 8.3) and data were fit to eq 18 and subsequently to eq 19, which afforded the apparent K_i values. [b]PfHGXPRT and HsHGPRT assays were performed at 25 °C (pH 7.4) and data were fit to eq 20. [c]The selectivity index (SI) was calculated as the K_i of HsHGPRT divided by the appK_i of T. cruzi HGPRT. [d]N.D.: not determined.

The acyclic forms of 8 and 9, which are 11 and 12, respectively (acyclic Immucillins[34,65−67]), show a roughly 4- and 3-fold increase in K_i, respectively, indicating that the 2′ and 3′ hydroxyl groups of 8 and 9 contribute to inhibitor binding. The addition of hydroxyl groups that are comparable to the 2′ hydroxyl of the ribose ring in compounds (S)-2 and 1 results in a roughly 55- and 240-fold decrease in the K_i value, respectively. The (S)-2 enantiomer binds roughly 40-fold tighter than the (R)-2 enantiomer, which demonstrates a strong preference for the chirality in this position. Furthermore, phosphonate (S)-2 bound to the enzyme significantly tighter than phosphate 7, as is evident by the 80-fold difference in K_i. Compounds (S)-2, (R)-2, 3, 5, 6, and 7 displayed a high selectivity index (SI) value (>8) for T. cruzi HGPRT vs HsHGPRT (Table 7), indicating their promise as antiparasitic compounds. The inhibitory activity of the Immucillins and acyclic analogues must also be ascertained against T. cruzi HGXPRTs isoforms (TcB and TcD), as the residual activity of either HGPRT or HGXPRT isoforms may suffice for the parasite's survival, according to in vitro studies in T. brucei.[31]

These results are a positive demonstration that TSAIs can be repurposed as potent inhibitors of a closely related target, as for the case of PfHGXPRT and T. cruzi HGPRTs. Even though PfHGXPRT adopts a tetrameric quaternary structure,[37] while T. cruzi HGPRTs are homodimers,[35] the apparent similarities of their active-site conformations and their inhibition by compounds that are structural mimics of an S_N1-TS structure encourage the assumption that the TS of the T. cruzi HGPRT is similar to that experimentally determined for PfHGXPRT.[45] To highlight this assumption, the most potent inhibitors for both enzymes show the same order of potency ((S)-2, 3, 8, and 6). These compounds vary in potency with K_i values ranging from 0.65 to 9 nM for PfHGXPRT, although higher K_i values of 13−180 nM were observed for the trypanosomal enzyme. The anticipated availability of crystallographic data of T. cruzi HGPRTs bound to TSAIs will provide a means to improve the potency and selectivity of TcC inhibitors by structural modifications of these first-generation compounds for the development of novel drugs specific for CD.

Hypothesis for *T. cruzi* HGPRT Inhibition Mechanism by TSAIs. The subset of Immucillins tested as *T. cruzi* HGPRT inhibitors all showed uncompetitive inhibition *vs* Hx (Figures S14 and S15), indicating that they bind to TcC after the binding of Hx and corroborating our data that TcC operates by a Bi Bi sequential ordered mechanism, where PRPP binds first to the free enzyme, followed by the 6-oxopurine base (Figures 2 and 3 and Table 3); therefore, the tested inhibitors bind to an enzyme form present after the E-PRPP-Hx complex is formed. Our reported viscosity effects on k_{cat}/K_{PRPP} indicated that a nonchemical step(s) is rate limiting for TcC catalysis (Figure 4), which we hypothesize to correspond to an isomerization event triggered by both substrates binding in which a flexible loop (loop II) closes over the active site, allowing the reaction to proceed according to a S_N1-like mechanism, where the post-chemistry step of active-site opening is slower than catalysis ($k_9 \ll k_7$) (Figure 2).

We suggest that in the presence of TSAIs, the conformational changes to one active site triggered by the binding of both substrates (closing of loop II over the active site of one subunit) allow the binding of an inhibitor molecule to the adjacent subunit, possibly due to induced conformational changes mediated by the inter-subunit Lys52−Met74 interaction. The available crystallographic data for *Pf*HGXPRT and *Hs*HGPRT show that these TSAIs bind to the PPRT active site in the presence of PPi, forming a E-PPi-I dead-end complex[37,79,87] (Figure S12, middle panel). The formation of E-PPi-Hx dead-end complexes has been previously proposed for TcA.[34] According to the proposed kinetic mechanism (Figure 2), product desorption follows an obligate order of PPi release prior to NMP, such that the dead-end inhibitor analogues of NMP may only bind to free HGPRT and not to complexes such as E-PRPP, E-PRPP-Purine, and E′-PPi-NMP (Figures 2, S14, and S15). The hypothesis of one active site from the HGPRT homodimer being occupied by substrates and eliciting a conformational change that promotes the binding of a TSAI molecule to the adjacent subunit explains the partial inhibition and cooperativity observed and conforms to our proposed reaction mechanism (Figures 2−5).

The catalytic characterization of TcC revealed that TcA and TcC enzymes are functionally equivalent. Initial velocity studies in the presence and absence of products, and the ITC binding assays provided evidence that TcC follows an ordered Bi Bi kinetic mechanism (Figures 2, 3, and S8−S10), as proposed for TcA.[34] We conclude that the trypanosomal HGPRT employs an S_N1-like mechanism, as described for *Pf*HGXPRT,[45] where the conformational change of the active-site loop II followed by release of the first product, PPi, corresponds to the rate-limiting step(s) of catalysis (Figures 4 and 5). We also showed the value of repurposing TSAIs developed as inhibitors of ortholog targets when both the active-site structure and reaction mechanisms are conserved (Chart 1 and Table 7), an approach that significantly accelerates the identification of potent lead candidates with selectivity over the human homologue, *Hs*HGPRT.

■ ASSOCIATED CONTENT

Ⓢ Supporting Information
The Supporting Information is available free of charge at https://pubs.acs.org/doi/10.1021/acs.biochem.2c00312.

> Additional experimental details, materials, and methods, including additional figures as indicated throughout the text (PDF)

Accession Codes
TcA: TcCLB.509693.70 (TriTrypDB), Q27796 (UniProt). TcC: TcCLB.506457.30 (TriTrypDB), Q27796 (UniProt). *Tbb*APRT1: Tbb927.7.1780 (TriTrypDB), Q57V32 (UniProt). *Sc*ADE: P53909 (UniProt). *Pf*HGXPRT: P20035 (UniProt). *Hs*HGPRT: P00492 (UniProt). *Sp*IMPDH: P0C0H6 (UniProt).

■ AUTHOR INFORMATION

Corresponding Authors
Thomas D. Meek − *Department of Biochemistry and Biophysics, Texas A&M University, College Station, Texas 77843-2128, United States*; Email: Thomas.Meek@ag.tamu.edu

Ardala Katzfuss − *Department of Biochemistry and Biophysics, Texas A&M University, College Station, Texas 77843-2128, United States*; ⓘ orcid.org/0000-0002-7177-9600; Email: ardalakatzfuss@gmail.com

Authors
Kayla Glockzin − *Department of Biochemistry and Biophysics, Texas A&M University, College Station, Texas 77843-2128, United States*; ⓘ orcid.org/0000-0003-2406-532X

Demetrios Kostomiris − *Department of Biochemistry and Biophysics, Texas A&M University, College Station, Texas 77843-2128, United States*; Present Address: R&D, AstraZeneca, 35 Gatehouse Drive, Waltham, Massachusetts 02451, United States

Yacoba V. T. Minnow − *Department of Biochemistry, Albert Einstein College of Medicine, Bronx, New York 10461-1602, United States*

Kajitha Suthagar − *Ferrier Research Institute, Victoria University of Wellington, Gracefield Research Centre, Lower Hutt 5010, New Zealand*

Keith Clinch − *Ferrier Research Institute, Victoria University of Wellington, Gracefield Research Centre, Lower Hutt 5010, New Zealand*

Sinan Gai − *Ferrier Research Institute, Victoria University of Wellington, Gracefield Research Centre, Lower Hutt 5010, New Zealand*; Present Address: Department of Chemistry, University of Otago, Science 2 Building, Dunedin 9016, New Zealand.

Joshua N. Buckler − *Ferrier Research Institute, Victoria University of Wellington, Gracefield Research Centre, Lower Hutt 5010, New Zealand*; ⓘ orcid.org/0000-0002-4397-9947

Vern L. Schramm − *Department of Biochemistry, Albert Einstein College of Medicine, Bronx, New York 10461-1602, United States*; ⓘ orcid.org/0000-0002-8056-1929

Peter C. Tyler − *Ferrier Research Institute, Victoria University of Wellington, Gracefield Research Centre, Lower Hutt 5010, New Zealand*; ⓘ orcid.org/0000-0002-3151-6208

Complete contact information is available at:
https://pubs.acs.org/10.1021/acs.biochem.2c00312

■ ACKNOWLEDGMENTS

■ ABBREVIATIONS

ADP:adenosine diphosphate; AMP:adenosine monophosphate; AMPS:adenylosuccinate; ATP:adenosine triphosphate; CD:Chagas disease; cpm:counts per minute; CV:column volume; dpm:disintegrations per minute; GDP:guanosine diphosphate; GMP:guanosine monophosphate; GTP:guanosine triphosphate; Gua:guanine; HGPRT:hypoxanthine—guanine phosphoribosyltransferase; HGXPRT:hypoxanthine—guanine—xanthine phosphoribosyltransferase; HPP:allopurinol (4-hydroxypyrazolo(3,4-d)pyrimidine); Hx:hypoxanthine; IMP:inosine monophosphate; IPTG:isopropyl β-D-1-thiogalactopyranoside; ITC:isothermal titration calorimetry; KIEs:kinetic isotope effects; LSC:liquid scintillation counting; OD:optical density; PNP:purine nucleoside phosphorylase; PPRT:phosphoribosyltransferase; M_r:relative molecular weight; MWCO:molecular weight cutoff; NMP:nucleoside monophosphate; PPi:pyrophosphate; PRPP:phospho-α-D-ribose-1-diphosphate; rpm:revolutions per minute; RT:room temperature; SDS-PAGE:sodium dodecyl sulfate-polyacrylamide gel electrophoresis; SEC:size-exclusion chromatography; TB media:terrific broth media; TcA/C:$T.$ $cruzi$ HGPRT isoforms; TS:transition-state; TSAIs:transition-state analogue inhibitors; Xan:xanthine; XO:xanthine oxidase; XMP:xanthosine monophosphate

■ REFERENCES

(1) Center for Disease Control. American Trypanosomiasis (also known as Chagas Disease). https://www.cdc.gov/parasites/chagas/gen_info/detailed.html#intro (accessed April 17, 2022).

(2) Pan American Health Organization. Chagas Disease. https://www.paho.org/en/topics/chagas-disease (accessed March 28, 2022).

(3) Bern, C.; Montgomery, S. P. An estimate of the burden of Chagas disease in the United States. *Clin. Infect. Dis.* **2009**, *49*, e52−e54.

(4) Perez-Molina, J. A.; Perez-Ayala, A.; Moreno, S.; Fernandez-Gonzalez, M. C.; Zamora, J.; Lopez-Velez, R. Use of benznidazole to treat chronic Chagas' disease: a systematic review with a meta-analysis. *J. Antimicrob. Chemother.* **2009**, *64*, 1139−1147.

(5) Braga, M. S.; Lauria-Pires, L.; Arganaraz, E. R.; Nascimento, R. J.; Teixeira, A. R. Persistent infections in chronic Chagas' disease patients treated with anti-*Trypanosoma cruzi* nitroderivatives. *Rev. Inst. Med. Trop. Sao Paulo* **2000**, *42*, 157−161.

(6) Urbina, J. A.; Docampo, R. Specific chemotherapy of Chagas disease: controversies and advances. *Trends Parasitol.* **2003**, *19*, 495−501.

(7) Bern, C. Chagas' Disease. *N. Engl. J. Med.* **2015**, *373*, 456−466.

(8) Herreros-Cabello, A.; Callejas-Hernandez, F.; Girones, N.; Fresno, M. *Trypanosoma cruzi* genome: organization, multi-gene families, transcription, and biological implication. *Genes* **2020**, *11*, No. 1196.

(9) Rassi, A., Jr.; Rassi, A.; Marcondes de Rezende, J. American trypanosomiasis (Chagas disease). *Infect. Dis. Clin. North Am.* **2012**, *26*, 275−291.

(10) Morillo, C. A.; Marin-Neto, J. A.; Avezum, A.; Sosa-Estani, S.; Rassi, A., Jr.; Rosas, F.; Villena, E.; Quiroz, R.; Bonilla, R.; Britto, C.; Guhl, F.; Velazquez, E.; Bonilla, L.; Meeks, B.; Rao-Melacini, P.; Pogue, J.; Mattos, A.; Lazdins, J.; Rassi, A.; Connolly, S. J.; Yusuf, S. Randomized trial of benznidazole for chronic Chagas' cardiomyopathy. *N. Engl. J. Med.* **2015**, *373*, 1295−1306.

(11) Bailey, F.; Eaton, J.; Jidda, M.; van Brakel, W. H.; Addiss, D. G.; Molyneux, D. H. Neglected Tropical Diseases and Mental Health: Progress, Partnerships, and Integration. *Trends Parasitol.* **2019**, *35*, 23−31.

(12) Engels, D.; Zhou, X. N. Neglected tropical diseases: an effective global response to local poverty-related disease priorities. *Infect. Dis. Poverty* **2020**, *9*, No. 10.

(13) de Oliveira, A. B. B.; Alevi, K. C. C.; Imperador, C. H. L.; Madeira, F. F.; de Azeredo-Oliveira, M. T. V. Parasite-Vector interaction of Chagas Disease: A mini review. *Am. J. Trop. Med. Hyg.* **2018**, *98*, 653−655.

(14) Moretti, N. S.; Mortara, R. A.; Schenkman, S. *Trypanosoma cruzi.* *Trends Parasitol.* **2020**, *36*, 404−405.

(15) Machado, F. S.; Dutra, W. O.; Esper, L.; Gollob, K.; Teixeira, M. N.; Factor, S. M.; Weiss, L. M.; Nagajyothi, F.; Tanowitz, H. B.; Garg, N. J. Current understanding of immunity to *Trypanosoma cruzi* infection and pathogenesis of Chagas Disease. *Semin. Immunopathol.* **2012**, *34*, 753−770.

(16) Nagajyothi, J. F.; Weiss, L. M. Advances in understanding the role of adipose tissue and mitochondrial oxidative stress in *Trypanosoma cruzi* infection. *F1000Research* **2019**, *8*, No. 1152.

(17) González, F. B.; Villar, S. R.; Toneatto, J.; Pacini, M. F.; Marquez, J.; D'Attilio, L.; Botasso, O. A.; Piwien-Pilipuk, G.; Perez, A. R. Immune response triggered by *Trypanosoma cruzi* infection strikes adipose tissue homeostasis altering lipid storage, enzyme profile and adipokine expression. *Med. Microbiol. Immunol.* **2019**, *208*, 651−666.

(18) Shikanai-Yasuda, M. A.; Carvalho, N. B. Oral transmission of Chagas Disease. *Clin. Infect. Dis.* **2012**, *54*, 845−852.

(19) Ramirez-Barrios, R.; Susa, E. K.; Smoniewski, C. M.; Faacks, S. P.; Ligget, C. K.; Zimmer, S. L. A link between mitochondrial gene expression and life stage morphologies in *Trypanosoma cruzi.* *Mol. Microbiol.* **2020**, *113*, 1003−1021.

(20) Oliveira, A. E. R.; Grazielle-Silva, V.; Ferreira, L. R. P.; Teixeira, S. M. R. Close encounters between *Trypanosoma cruzi* and the host mammalian cell: Lessons from genome-wide expression studies. *Genomics* **2020**, *112*, 990−997.

(21) Castillo, C.; Carrillo, I.; Libisch, G.; Juiz, N.; Schijman, A.; Robello, C.; Kemmerling, U. Host-parasite interaction: changes in human placental gene expression induced by *Trypanosoma cruzi.* *Parasites Vectors* **2018**, *11*, No. 479.

(22) Paes, M. C.; Saraiva, F. M. S.; Nogueira, N. P.; Vieira, C. S. D.; Dias, F. A.; Rossini, A.; Coelho, V. L.; Pane, A.; Sang, F.; Alcocer, M. Gene expression profiling of *Trypanosoma cruzi* in the presence of heme points to glycosomal metabolic adaptation of epimastigotes inside the vector. *PLoS Neglected Trop. Dis.* **2020**, *14*, No. e0007945.

(23) Lewis, M. D.; Llewellyn, M. S.; Gaunt, M. W.; Yeo, M.; Carrasco, H. J.; Miles, M. A. Flow cytometric analysis and microsatellite genotyping reveal extensive DNA content variation in *Trypanosoma cruzi* populations and expose contrasts between natural and experimental hybrids. *Int J Parasitol.* **2009**, *39*, 1305−1317.

(24) Berens, R. L.; Marr, J. J.; LaFon, S. W.; Nelson, D. J. Purine metabolism in *Trypanosoma cruzi.* *Mol. Biochem. Parasitol.* **1981**, *3*, 187−196.

(25) de Koning, H. P.; Bridges, D. J.; Burchmore, R. J. Purine and pyrimidine transport in pathogenic protozoa: from biology to therapy. *FEMS Microbiol. Rev.* **2005**, *29*, 987−1020.

(26) Sinha, S. The PRT protein family. *Curr. Opin. Struct. Biol.* **2001**, *11*, 733−739.

(27) Murta, S. M. F.; Gazzinelli, R. T.; Brener, Z.; Romanha, A. J. Molecular characterization of susceptible and naturally resistant strains

of *Trypanosoma cruzi* to benznidazole and nifurtimox. *Mol. Biochem. Parasitol.* **1998**, *93*, 203−214.

(28) Valsecchi, W. M.; Delfino, J. M.; Santos, J.; Villamil, S. H. F. Zoledronate repositioning as a potential trypanocidal drug. *Trypanosoma cruzi* HPRT an alternative target to be considered. *Biochem. Pharmacol.* **2021**, *188*, No. 114524.

(29) Soeiro, M. N. C.; de Castro, S. L. *Trypanosoma cruzi* targets for new chemotherapeutic approaches. *Expert Opin. Ther. Targets* **2009**, *13*, 105−121.

(30) Duschak, V. G.; Couto, A. S. An insight on targets and patented drugs for chemotherapy of Chagas Disease. *Recent Pat. Anti-Infect. Drug Discovery* **2007**, *2*, 19−51.

(31) Dolezelova, E.; Teran, D.; Gahura, O.; Kotrbova, Z.; Prochazkova, M.; Keough, D.; Spacek, P.; Hockova, D.; Guddat, L.; Zikova, A. Evaluation of the *Trypanosoma brucei* 6-oxopurine salvage pathway as a potential target for drug discovery. *PLoS Neglected Trop. Dis.* **2018**, *12*, No. e0006301.

(32) El-Sayed, N. M.; Myler, P. J.; Bartholomeu, D. C.; Nilsson, D.; Aggarwal, G.; Tran, A. N.; Ghedin, E.; Worthey, E. A.; Delcher, A. L.; Blandin, G.; Westenberger, S. J.; Caler, E.; Cerqueira, G. C.; Branche, C.; Haas, B.; Anupama, A.; Arner, E.; Aslund, L.; Attipoe, P.; Bontempi, E.; Bringaud, F.; Burton, P.; Cadag, E.; Campbell, D. A.; Carrington, M.; Crabtree, J.; Darban, H.; da Silveira, J. F.; de Jong, P.; Edwards, K.; Englund, P. T.; Fazelina, G.; Feldblyum, T.; Ferella, M.; Frasch, A. C.; Gull, K.; Horn, D.; Hou, L.; Huang, Y.; Kindlund, E.; Klingbeil, M.; Kluge, S.; Koo, H.; Lacerda, D.; Levin, M. J.; Lorenzi, H.; Louie, T.; Machado, C. R.; McCulloch, R.; McKenna, A.; Mizuno, Y.; Mottram, J. C.; Nelson, S.; Ochaya, S.; Osoegawa, K.; Pai, G.; Parsons, M.; Pentony, M.; Pettersson, U.; Pop, M.; Ramirez, J. L.; Rinta, J.; Robertson, L.; Salzberg, S. L.; Sanchez, D. O.; Seyler, A.; Sharma, R.; Shetty, J.; Simpson, A. J.; Sisk, E.; Tammi, M. T.; Tarleton, R.; Teixeira, S.; Van Aken, S.; Vogt, C.; Ward, P. N.; Wickstead, B.; Wortman, J.; White, O.; Fraser, C. M.; Stuart, K. D.; Andersson, B. The genome sequence of *Trypanosoma cruzi*, etiologic agent of Chagas disease. *Science* **2005**, *309*, 409−415.

(33) Allen, T. E.; Ullman, B. Molecular characterization and overexpression of the hypoxanthine-guanine phosphoribosyltransferase gene from *Trypanosoma cruzi*. *Mol. Biochem. Parasitol.* **1994**, *65*, 233−245.

(34) Wenck, M. A.; Medrano, F. J.; Eakin, A. E.; Craig, S. P. Steady-state kinetics of the hypoxanthine phosphoribosyltransferase from *Trypanosoma cruzi*. *Biochim. Biophys. Acta, Proteins Proteomics* **2004**, *1700*, 11−18.

(35) Focia, P. J.; Craig, S. P., 3rd; Eakin, A. E. Approaching the transition state in the crystal structure of a phosphoribosyltransferase. *Biochemistry* **1998**, *37*, 17120−17127.

(36) Clinch, K.; Evans, G. B.; Frohlich, R. F.; Furneaux, R. H.; Kelly, P. M.; Legentil, L.; Murkin, A. S.; Li, L.; Schramm, V. L.; Tyler, P. C.; Woolhouse, A. D. Third-generation immucillins: syntheses and bioactivities of acyclic immucillin inhibitors of human purine nucleoside phosphorylase. *J. Med. Chem.* **2009**, *52*, 1126−1143.

(37) Hazleton, K. Z.; Ho, M. C.; Cassera, M. B.; Clinch, K.; Crump, D. R.; Rosario, I., Jr.; Merino, E. F.; Almo, S. C.; Tyler, P. C.; Schramm, V. L. Acyclic immucillin phosphonates: second-generation inhibitors of *Plasmodium falciparum* hypoxanthine-guanine-xanthine phosphoribosyltransferase. *Chem. Biol.* **2012**, *19*, 721−730.

(38) Keough, D.; Ng, A.-L.; Winzor, D.; Emmerson, B.; de Jersey, J. Purification and characterization of *Plasmodium falciparum* hypoxanthine−guanine−xanthine phosphoribosyltransferase and comparison with the human enzyme. *Mol. Biochem. Parasitol.* **1999**, *98*, 29−41.

(39) Cheviet, T.; Lefebvre-Tournier, I.; Wein, S.; Peyrottes, S. Plasmodium purine metabolism and its inhibition by nucleoside and nucleotide analogues. *J. Med. Chem.* **2019**, *62*, 8365−8391.

(40) Munagala, N.; Sarver, A. E.; Wang, C. C. Converting the guanine phosphoribosyltransferase from *Giardia lamblia* to a hypoxanthine-guanine phosphoribosyltransferase. *J. Biol. Chem.* **2000**, *275*, 37072−37077.

(41) Pundir, C. S.; Devi, R.; Narang, J.; Singh, S.; Nehra, J.; Chaudhry, S. Fabrication of an amperometric xanthine biosensor based on polyvinylchloride membrane. *J. Food Biochem.* **2012**, *36*, 21−27.

(42) Origin; OriginLab Corporation: Northampton, MA.

(43) Gadda, G.; Sobrado, P. Kinetic solvent viscosity effects as probes for studying the mechanisms of enzyme action. *Biochemistry* **2018**, *57*, 3445−3453.

(44) Glockzin, K.; Meek, T. D.; Katzfuss, A. Characterization of adenine phosphoribosyltransferase (APRT) activity in *Trypanosoma brucei brucei:* Only one of the two isoforms is kinetically active. *PLoS Neglected Trop. Dis.* **2022**, *16*, No. e0009926.

(45) Ducati, R. G.; Firestone, R. S.; Schramm, V. L. Kinetic isotope effects and transition state structure for hypoxanthine-guanine-xanthine phosphoribosyltransferase from *Plasmodium falciparum*. *Biochemistry* **2017**, *56*, 6368−6376.

(46) Edler, R. *Available Quench Parameters in TriCarb LSC's*; PerkinElmer, Inc., 2015.

(47) Rose, I. A.; O'Connell, E. L.; O'Connell, E. L.; Litwin, S. Determination of the rate of hexokinase-glucose dissociation by the isotope-trapping method. *J. Biol. Chem.* **1974**, *249*, 5163−5168. From NLM

(48) Rose, I. A. The Isotope Trapping Method: Desorption Rates of Productive E.S Complexes. In *Enzyme Kinetics and Mechanism—Part B: Isotopic Probes and Complex Enzyme Systems*; Purich, D. L., Ed.; Methods in Enzymology; Elsevier B.V., 1980; Vol. *64*, pp 47−59. From NLM Medline

(49) Cook, P. F.; Cleland, W. W. *Enzyme Kinetics and Mechanism*; Garland Science, 2007.

(50) O'Leary, M. H.; Marlier, J. F. Heavy-atom isotope effects on the alkaline hydrolysis and hydrazinolysis of methyl benzoate. *J. Am. Chem. Soc.* **1979**, *101*, 3300−3306.

(51) Contreras-Sanz, A.; Scott-Ward, T. S.; Gill, H. S.; Jacoby, J. C.; Birch, R. E.; Malone-Lee, J.; Taylor, K. M.; Peppiatt-Wildman, C. M.; Wildman, S. S. Simultaneous quantification of 12 different nucleotides and nucleosides released from renal epithelium and in human urine samples using ion-pair reversed-phase HPLC. *Purinergic Signalling* **2012**, *8*, 741−751.

(52) Clinch, K.; Crump, D. R.; Evans, G. B.; Hazleton, K. Z.; Mason, J. M.; Schramm, V. L.; Tyler, P. C. Acyclic phosph(on)ate inhibitors of *Plasmodium falciparum* hypoxanthine-guanine-xanthine phosphoribosyltransferase. *Bioorg. Med. Chem.* **2013**, *21*, 5629−5646.

(53) Li, C. M.; Tyler, P. C.; Furneaux, R. H.; Kicska, G.; Xu, Y.; Grubmeyer, C.; Girvin, M. E.; Schramm, V. L. Transition-state analogs as inhibitors of human and malarial hypoxanthine-guanine phosphoribosyltransferases. *Nat. Struct. Biol.* **1999**, *6*, 582−587.

(54) Copeland, R. A. *Evaluation of Enzyme Inhibitors in Drug Discovery: A Guide for Medicinal Chemists and Pharmacologists*; Wiley-Interscience, 2005.

(55) Kramers, H. A. Brownian motion in a field of force and the diffusion model of chemical reactions. *Physica* **1940**, *7*, 284−304.

(56) Raber, M. L.; Freeman, M. F.; Townsend, C. A. Dissection of the stepwise mechanism to β-lactam formation and elucidation of a rate-determining conformational change in β-lactam synthetase. *J. Biol. Chem.* **2009**, *284*, 207−217.

(57) Cheng, Y. C.; Prusoff, W. H. Relationship between the inhibition constant (K_i) and the concentration of inhibitor which causes 50 per cent inhibition (I_{50}) of an enzymatic reaction. *Biochem. Pharmacol.* **1973**, *22*, 3099−3108.

(58) Grant, S. K.; Moore, M. L.; Fakhoury, S. A.; Tomaszek, T. A.; Meek, T. D. Inactivation of HIV-1 protease by a tripeptidyl epoxide. *Bioorg. Med. Chem. Lett.* **1992**, *2*, 1441−1445.

(59) Marr, J. J.; Berens, R. L. Pyrazolopyrimidine metabolism in the pathogenic trypanosomatidae. *Mol. Biochem. Parasitol.* **1983**, *7*, 339−356.

(60) Eakin, A. E.; Guerra, A.; Focia, P. J.; Torres-Martinez, J.; Craig, S. P., 3rd. Hypoxanthine phosphoribosyltransferase from *Trypanosoma cruzi* as a target for structure-based inhibitor design: crystallization and inhibition studies with purine analogs. *Antimicrob. Agents Chemother.* **1997**, *41*, 1686−1692.

(61) Canyuk, B.; Focia, P. J.; Eakin, A. E. The role for an invariant aspartic acid in hypoxanthine phosphoribosyltransferases is examined using saturation mutagenesis, functional analysis, and X-ray crystallography. *Biochemistry* **2001**, *40*, 2754−2765.

(62) Canyuk, B.; Medrano, F. J.; Wenck, M. A.; Focia, P. J.; Eakin, A. E.; Craig, S. P., 3rd. Interactions at the dimer interface influence the relative efficiencies for purine nucleotide synthesis and pyrophosphorolysis in a phosphoribosyltransferase. *J. Mol. Biol.* **2004**, *335*, 905−921.

(63) Segel, I. H. *Enzyme Kinetics—Behavior and Analysis of Rapid Equilibrium and Steady-State Enzyme Systems*; Wiley Interscience Publication, 1993.

(64) Velazquez-Campoy, A.; Kiso, Y.; Freire, E. The binding energetics of first- and second-generation HIV-1 protease inhibitors: implications for drug design. *Arch. Biochem. Biophys.* **2001**, *390*, 169−175.

(65) Xu, Y.; Eads, J.; Sacchettini, J. C.; Grubmeyer, C. Kinetic mechanism of human hypoxanthine-guanine phosphoribosyltransferase: rapid phosphoribosyl transfer chemistry. *Biochemistry* **1997**, *36*, 3700−3712.

(66) Roy, S.; Nagappa, L. K.; Prahladarao, V. S.; Balaram, H. Kinetic mechanism of *Plasmodium falciparum* hypoxanthine-guanine-xanthine phosphoribosyltransferase. *Mol. Biochem. Parasitol.* **2015**, *204*, 111−120.

(67) Bashor, C.; Denu, J. M.; Brennan, R. G.; Ullman, B. Kinetic mechanism of adenine phosphoribosyltransferase from *Leishmania donovani*. *Biochemistry* **2002**, *41*, 4020−4031.

(68) Nakatani, H.; Dunford, H. B. Meaning of diffusion-controlled association rate constants in enzymology. *J. Phys. Chem. A* **1979**, *83*, 2662−2665.

(69) Cerjan, C.; Barnett, R. E. Viscosity dependence of a putative diffusion-limited reaction. *J. Phys. Chem. B* **1972**, *76*, 1192−1195.

(70) Brouwer, A. C.; Kirsch, J. F. Investigation of diffusion-limited rates of chymotrypsin reactions by viscosity variation. *Biochemistry* **1982**, *21*, 1302−1307.

(71) Munagala, N.; Basus, V. J.; Wang, C. C. Role of the flexible loop of hypoxanthine-guanine-xanthine phosphoribosyltransferase from *Tritrichomonas foetus* in enzyme catalysis. *Biochemistry* **2001**, *40*, 4303−4311.

(72) Focia, P. J.; Craig, S. P., 3rd; Nieves-Alicea, R.; Fletterick, R. J.; Eakin, A. E. A 1.4 A crystal structure for the hypoxanthine phosphoribosyltransferase of *Trypanosoma cruzi*. *Biochemistry* **1998**, *37*, 15066−15075.

(73) Breda, A.; Rosado, L. A.; Lorenzini, D. M.; Basso, L. A.; Santos, D. S. Molecular, kinetic and thermodynamic characterization of *Mycobacterium tuberculosis* orotate phosphoribosyltransferase. *Mol. BioSyst.* **2012**, *8*, 572−586.

(74) Wang, G. P.; Cahill, S. M.; Liu, X.; Girvin, M. E.; Grubmeyer, C. Motional dynamics of the catalytic loop in OMP synthase. *Biochemistry* **1999**, *38*, 284−295.

(75) Lee, C. C.; Medrano, F. J.; Craig, S. P.; Eakin, A. E. Investigation of the functional role of active site loop II in a hypoxanthine phosphoribosyltransferase. *Biochim. Biophys. Acta, Mol. Basis Dis.* **2001**, *1537*, 63−70.

(76) Cleland, W. W. Enzyme Mechanisms from Isotope Effects. In *Isotope Effects in Chemistry and Biology*; Limbach, A. K. H.-H., Ed.; Taylor & Francis, 2006; pp 915−930.

(77) Cook, P. F.; Cleland, W. W. Mechanistic deductions from isotope effects in multireactant enzyme mechanisms. *Biochemistry* **1981**, *20*, 1790−1796.

(78) Goitein, R. K.; Chelsky, D.; Parsons, S. M. Primary ^{14}C and α secondary ^{3}H substrate kinetic isotope effects for some phosphoribosyltransferases. *J. Biol. Chem.* **1978**, *253*, 2963−2971.

(79) Shi, W.; Li, C. M.; Tyler, P. C.; Furneaux, R. H.; Grubmeyer, C.; Schramm, V. L.; Almo, S. C. The 2.0 Å structure of human hypoxanthine-guanine phosphoribosyltransferase in complex with a transition-state analog inhibitor. *Nat. Struct. Biol.* **1999**, *6*, 588−593.

(80) Lewandowicz, A.; Schramm, V. L. Transition state analysis for human and *Plasmodium falciparum* purine nucleoside phosphorylases. *Biochemistry* **2004**, *43*, 1458−1468.

(81) Berti, P. J.; McCann, J. A. Toward a detailed understanding of base excision repair enzymes: transition state and mechanistic analyses of N-glycoside hydrolysis and N-glycoside transfer. *Chem. Rev.* **2006**, *106*, 506−555. From NLM Medline

(82) Kicska, G. A.; Tyler, P. C.; Evans, G. B.; Furneaux, R. H.; Kim, K.; Schramm, V. L. Transition state analogue inhibitors of purine nucleoside phosphorylase from *Plasmodium falciparum*. *J. Biol. Chem.* **2002**, *277*, 3219−3225.

(83) Miles, R. W.; Tyler, P. C.; Furneaux, R. H.; Bagdassarian, C. K.; Schramm, V. L. One-third-the-sites transition-state inhibitors for purine nucleoside phosphorylase. *Biochemistry* **1998**, *37*, 8615−8621.

(84) Taylor, E. A.; Clinch, K.; Kelly, P. M.; Li, L.; Evans, G. B.; Tyler, P. C.; Schramm, V. L. Acyclic ribooxacarbenium ion mimics as transition state analogues of human and malarial purine nucleoside phosphorylases. *J. Am. Chem. Soc.* **2007**, *129*, 6984−6985.

(85) Keough, D. T.; Brereton, I. M.; Jersey, J.; Guddat, L. W. The crystal structure of free human hypoxanthine-guanine phosphoribosyltransferase reveals extensive conformational plasticity throughout the catalytic cycle. *J. Mol. Biol.* **2005**, *351*, 170−181.

(86) Ho, M. C.; Shi, W.; Rinaldo-Matthis, A.; Tyler, P. C.; Evans, G. B.; Clinch, K.; Almo, S. C.; Schramm, V. L. Four generations of transition-state analogues for human purine nucleoside phosphorylase. *Proc. Natl. Acad. Sci. U.S.A.* **2010**, *107*, 4805−4812. From NLM Medline

(87) Shi, W.; Li, C. M.; Tyler, P. C.; Furneaux, R. H.; Cahill, S. M.; Girvin, M. E.; Grubmeyer, C.; Schramm, V. L.; Almo, S. C. The 2.0 Å structure of malarial purine phosphoribosyltransferase in complex with a transition-state analogue inhibitor. *Biochemistry* **1999**, *38*, 9872−9880.